

LIGHT EMITTING MATERIALS AND CONTROL OF
THEIR EMISSION PROPERTIES FOR APPLICATIONS
IN INTEGRATED OPTICS

A Dissertation

Presented to the Faculty of the Graduate School

of Cornell University

in Partial Fulfillment of the Requirements for the Degree of

Doctor of Philosophy

by

Carl Bernard Poitras

August 2006

© 2006 Carl Bernard Poitras

ALL RIGHTS RESERVED

LIGHT EMITTING MATERIALS AND CONTROL OF THEIR EMISSION
PROPERTIES FOR APPLICATIONS IN INTEGRATED OPTICS

Carl Bernard Poitras, Ph.D.

Cornell University 2006

The field of nanophotonics has had numerous great achievements in the past few years (for a brief overview, see [1]). The scaling down of optical devices has created a need for active, light emitting materials whose properties need to be controlled for usage at such small scales. This dissertation presents results on the control of the emission of different light emitting materials. Chapter one presents a brief discussion of active materials for on-chip applications, what they are and their uses.

Chapter two deals with the enhancement of CdSe quantum dots embedded in a microcavity. After a brief overview of the density of photon modes and how enhancement can be achieved, the experimental details and results are presented, showing enhancement of the photoluminescence of the quantum dots by a factor of 2.7.

The third chapter discusses experiments with CdSe dots and resonant energy transfer. This effect involves a donor and an acceptor in close proximity, with the former "giving" its energy to the latter. The emission of the acceptor is further enhanced by making use of a microcavity, with a total enhancement by a factor of 13.

Experimental results on rare earth doped GaN in the form of a powder are

presented in chapter four. This type of material presents highly luminescent properties, and offers the flexibility of being used in a hybrid manner (on silicon for example). Cathodoluminescence, photoluminescence and lifetime properties of various concentrations of RE dopants are discussed and presented, as well as a visible waveguide application of Eu doped GaN powder. Two temperature-sensitive changes in the lifetime behavior of Eu doped GaN occur at 104 and 195 K. The lifetime dynamics are studied in greater detail using a model with corresponding rate equations.

The last chapter shows applications of another class of a light emitting material: silica clad organic dyes. These particles have a promising future in applications such as labeling and sensing.

Even though the materials studied here emit light in the visible portion of the spectrum, all of the experiments herein contained can be realized with their infrared counterparts.

BIOGRAPHICAL SKETCH

Carl Poitras grew up in and near Montréal, Québec, Canada. Carl began his undergraduate studies at the Université du Québec à Montréal in microelectronics and completed them by obtaining his bachelor's degree in physics. Carl went on to complete one year at the master's level in physics in electromagnetism, also at the Université du Québec à Montréal, and switched fields to obtain his master's degree in telecommunications from the Institut National de Recherche Scientifique (INRS) in Montréal.

His passion for physics, and electromagnetism in particular, led Carl to join Professor Michal Lipson's nanophotonics group at Cornell in fall 2001. The main focus of his studies as a Ph.D. student at Cornell involved the study and applications of light emitting materials for nanophotonics.

ACKNOWLEDGEMENTS

My nearly five year experience as a Ph.D. student at Cornell University in the nanophotonics group has enriched my life in many different ways. The interactions with students and professors have led to a very humbling experience, where everyone was and continues to be united for the purpose of learning and furthering scientific knowledge. This kind of environment is a nurturing one, and I am fortunate to have had the opportunity to complete a Ph.D. at Cornell University.

There are so many reasons for which I wish to thank my advisor, Professor Michal Lipson. Her enthusiasm, resourcefulness, intelligence and insight have and continue to be a great inspiration for me. I was very fortunate to have been part of her research group.

I also wish to thank Professor Clifford Pollock for his support throughout my studies. His knowledge and expertise in the laboratory environment make him a resourceful person with whom it is a pleasure to work.

Discussions with Professor Frank Wise have proven to be greatly useful and insightful with regard to the completion of my doctoral studies. His command of the physical sciences make him an excellent communicator and instructor, and learning from him was a pleasure.

The collaborators without whom my research projects would not have even taken form certainly deserve my thanks. It was, and continues to be, a pleasure to work with these wonderful people. Prof. Todd K. Krauss from the department of chemistry at the University of Rochester was directly involved with the experiments with the quantum dots. Prof. Krauss' students, Hui Du, Megan A. Hahn and Li Guo, have made the experiment on photoluminescence enhancement a possibility. Xiao Teng and Prof. Hong Yang from the department of chemical

engineering, also at the University of Rochester, were part of the team with regard to the energy transfer experiments between colloidal quantum dots. I also extend my warmest thanks to Prof. Michael G. Spencer from Cornell University and his former student Huaqiang Wu for the experiments on the rare earth doped GaN powder. Janet Hunting and Francis J. DiSalvo were also involved with the GaN powder experiments. Lastly, I wish to thank Prof. Ulrich Wiesner from the department of materials science and engineering at Cornell along with his student Andrew Burns for making the experiments on the CU dots possible.

I wish to thank Prof. Elie Boridy, a physics professor at the Université du Québec à Montréal. Elie is an outstanding physics teacher who sparked my interest in the physical sciences. He has been and continues to be a great friend, and he is the reason why I have undertaken and completed a Ph.D.

My parents deserve my admiration and thanks. They have continuously encouraged me in all of my endeavors, and have been proud no matter what the outcome. My sister and brother have been as supportive as ever, always wishing the best for me, and I thank them.

I wish to thank my friend Tameem Albash for his friendship, wits, and patience. Our good physics discussions have been and continue to be helpful and enlightening.

There is great synergy between all of the members of Prof. Lipson's group, and this leads to a most conducive environment to learn and perform research. Everyone interacts with one another, bringing insight, expertise and, when needed, encouragement. For these reasons, I first wish to thank Wilson R. Almeida, who was of guidance to me at the onset of my studies. I also extend my warmest thanks to Carlos Barrios, Richard Brown, Joel Buckley, Long Chen, Po Dong, Stephen Emelett,

Alexander (Sasha) Gondarenko, Sasikanth Manipatruni, Christina Manolatu, Linnell Martinez, Roberto Panepucci, Sameer Pradhan, Stefan Preble, Jacob Robinson, Bradley Schmidt, Jagat Shakya, Amy Turner, Morgan Winer, and Qianfan Xu.

TABLE OF CONTENTS

1	Active Materials for On-Chip Applications	1
2	Photoluminescence Enhancement and Inhibition Colloidal Quantum Dots	3
2.1	Introduction	3
2.2	Photoluminescence Enhancement	5
2.2.1	Density of Photon Modes	5
2.2.2	Experiment and Results	13
3	Förster Energy Transfer in Colloidal Quantum Dots	27
3.1	Introduction	27
3.2	Quantum Electrodynamic Description of Förster Resonant Energy Transfer	28
3.3	Experiment and Results	39
4	Rare Earth doped GaN in the form of a powder	46
4.1	Introduction	46
4.2	Er doped GaN Powder - Experiment and Results	48
4.3	Eu doped GaN Powder - Experiment and Results	51
4.3.1	Lifetime Dynamics and Waveguide Application	56
5	Applications of Fluorescing Core-Shell Silica Nanoparticles (CU Dots)	69
5.1	Introduction	69
5.2	Experiments and Results	69

A Evaluation of the Green function in the QED treatment of FRET	76
Bibliography	80
Bibliography	81

LIST OF FIGURES

2.1	Electromagnetic fields of a linearly polarized wave propagating across the boundaries between three thin films.	8
2.2	Intensity ($ E ^2$) of the field throughout a microcavity with six pairs of $\lambda/4n$ layers of alternating indices of refraction with a $\lambda/2n$ microcavity. The light grey regions represent a material with higher index of refraction than the dark grey regions.	10
2.3	Calculated transmission spectra, for $\lambda_0 = 552.7$ nm, of stacks of quarter wavelength ($\lambda_0/4n$) films of alternating indices of refraction ($n_H = 2.1$ and $n_L = 1.46$) in the case of (a) , a six pair DBR of n_H - n_L layers; and (b) , a $\lambda_0/2n_L$ microcavity formed between two DBRs with reflection spectra as shown in (a) . The dotted line represents qualitatively the DOM in 1D free space.	12
2.4	Free space photoluminescence of the CdSe NCs used in the experiment under the 457.9 nm laser line of an argon laser.	14
2.5	3D schematic representation of the final structure, with its wedged characteristic. Thicker film regions have a correspondingly higher wavelength resonance (top spectrum), while thinner film regions have a lower wavelength resonance (bottom spectrum).	17
2.6	Measured transmission of the monolithic Fabry-Pérot microcavity embedded with NCs. Superimposed is the free space photoluminescence spectrum of the reference sample.	19
2.7	(a) Experimental and theoretical transmission spectra for three different cavity resonances. (b) Calculated absorption of the cavity and reference samples as a function of wavelength.	21

2.8	Photoluminescence of the NCs from within the microcavity on and off resonance (dotted and dashed lines respectively) with the emission peak of the NCs in the reference sample (solid line).	22
2.9	Position of the cavity's resonance as a function of the collection angle θ . The square symbols represent the experimental measurements, while the other two are theoretical: the triangles represent the transfer matrix method simulations, and the dashed line the formula derived below (see equation 2.18). The inset shows how the angle θ is measured with respect to the sample.	23
2.10	Simple schematic for the calculation of the blue shift of the cavity's resonance as a function of the collection angle θ	24
3.1	Feynman diagrams showing the two time orderings involved in resonant energy transfer (dipole-dipole), where 0 is the ground state level, α and β are the excited state levels for the Acceptor and Donor respectively. The virtual photon has momentum \mathbf{p} and polarization λ . Time flows from left to right. (a) Case where the Donor is first excited and energy is subsequently transferred to the Acceptor. (b) Case where the Acceptor is first excited (see text).	33
3.2	Photoluminescence and absorption spectra of the two different sized NCs that were used in the FRET experiment (from [66]).	39
3.3	Free space photoluminescence spectra of: a colloidal suspension of mixed NCs (solid line), a monolayer of mixed NCs (open circles), and a monolayer of the larger (4.6 nm) NCs only (triangles) (from [66]).	40

3.4	Normalized fluorescence spectra from monolayers of NCs. The open circles represent the photoluminescence of large dots in free space. The solid line is the photoluminescence from the large NCs only inside a microcavity. The dashed line represents the photoluminescence from the mixed NCs inside a microcavity (from [66]).	42
4.1	Representative X-ray diffraction pattern for the case of the GaN:Er powder after the removal of Bi. All of the peaks match with the wurtzite GaN structure, and no traces of Ga, Bi or Er is detected (from [91]).	48
4.2	Scanning electron microscopy image of the morphology of the synthesized GaN:Er powder; particle sizes range from 1 to 5 μm and platelet particles are the majority (from [91]).	49
4.3	Room temperature photoluminescence spectrum of the Er doped GaN powder. The emissions at 537 and 558 nm are characteristic of $4f$ inner shell transitions in the Er^{3+} ions (from [91]).	50
4.4	SEM images of the Eu doped GaN powder (2 at.%). The top picture shows the overall morphology of the powder, while the lower picture is a zoom showing the highly faceted and hexagonal structure of the particles (from [90]).	51
4.5	Room temperature photoluminescence spectra of the GaN powder doped with Eu (1 at.%). The dark line corresponds to the emission from the above bandgap excitation (325 nm), while the gray line is the emission from the below bandgap excitation (457.9 nm) (from [90]).	53

4.6	Room temperature photoluminescence spectra of the GaN powder doped with different concentrations of Eu^{3+} (from [90]).	54
4.7	Room temperature cathodoluminescence of the GaN powder doped with a concentration of Eu^{3+} ions of 1 at.% (from [90]).	56
4.8	Lifetime decay curve (solid line) and double exponential fit (circles) of the 621 nm line of the Eu doped GaN powder (from [93]).	58
4.9	Temperature dependence of the lifetimes as a function of temperature obtained from best fits of equation 4.1 to the time decay curves from TRPL of the europium doped GaN powder. The two arrows indicate the temperatures at which the lifetime components undergo a change, one at 185 K and the other at 104 K (from [93]).	59
4.10	Schematic of the excitation and energy transfer processes model used for GaN:Eu (from [98]).	61
4.11	Time decay parameters obtained by best fits of the differential equations 4.2 to the lifetime measurements on the 621 nm line of the Eu doped GaN powder. (a) Energy transfer constant from the host (GaN) to the Eu ions. (b) Decay constant of the Eu ions at 621 nm. (c) Decay constants from the Eu ions to the trap (τ_{EI}) and from the trap to the Eu ions (τ_{IE}).	62
4.12	Schematic cross-section of an SiON waveguide along with the simulated TE fundamental mode at 621 nm. (a) TE mode of the SiON waveguide only, assuming $n = 1.53$. (b) TE mode in the GaN film which coats the waveguides, assuming $n = 1.53$ for the SiON and $n = 2.3$ for the GaN powder (from [93]).	67

5.1	Photoluminescence spectrum of the TRITC CU Dots used in the experiments. The 457.9 nm laser line of an Argon laser was used for the excitation.	70
5.2	Photoluminescence spectra of the TRITC CU Dots from within the microcavity. Three spectra are shown as taken from three different positions on the sample.	72
5.3	Time decay of the photoluminescence of the CU dots from within the microcavity (on resonance) The graph shows the experimental measurements (solid line) as well as a double exponential fit (open circles).	73
5.4	Pictures of Ar laser light at 457.9 nm guided in an SiON waveguide with CU dots on top of the waveguide. The pictures were taken (a) without any filtering, showing the guiding of the laser light, and (b) with filtering in order to prevent the Ar light from entering the camera, revealing the glowing CU dots.	75
A.1	Adequate contour for the integration of equation A.1 (for the e^{ipR} term).	77

CHAPTER 1

ACTIVE MATERIALS FOR ON-CHIP APPLICATIONS

The field of nanophotonics has but flourished in the past few years. The need for faster ways to transmit data has led to making use of light signals at a much smaller scale than the successful applications of fiber optics, which has resulted in the development of cutting-edge photonic devices (for an overview, see [1]). In so doing, a need for active materials at such small scales has led to studying various light emitting materials and the control of the emission properties.

In order to use light emitting materials at a nanoscale, control must be exerted over their emission, whether it is spatial control and/or control over the luminescence. A light emitter in its simplest form can be modeled as an electric dipole, with its characteristic donut shaped emission pattern into free space. Light emitting materials can be composed of a huge number of these dipole emitters, and the overall emission from an enormous number these light emitters is uniform radiation over a solid angle of 4π steradians. The small scale (from a few nanometers to possibly tens or hundreds of micrometers) nature of photonics is such that control over the uniform emission pattern just described must be exercised so that this radiation can be put to use for photonic applications in waveguides, splitters, resonators, etc.

Another important point has to do with the photoluminescence characteristics of the light emitting material. It would be greatly desirable to control these characteristics for the purpose of enhancing or inhibiting the emission of the light, and possibly get lasing. In fact, the importance of exerting control over the emission of light emitting materials is such that, at the time of the publication of this dissertation, a large-scale DoD funded collaboration between several universities in

the United States was initiated to develop a silicon laser for all-optical on-chip integrated systems.

As will be seen in the following chapters, much has been accomplished in order to exert control over all sorts of light emitters. This dissertation is on this very topic, where several types of light emitters are analyzed and whose luminescence characteristics are enhanced and suppressed. One key component at the heart of this exercise of the control of the emission properties is a microcavity, which can be engineered to enhance the emission of radiation at given wavelengths while suppressing such emission at other wavelengths. Various light emitting materials are considered here: colloidal CdSe visible light emitting nanocrystals, whose emission is enhanced and suppressed as shown in the following two chapters, with chapter 2 describing light emission enhancement and inhibition, and chapter 3 presenting results on Förster resonant energy transfer between two sizes of nanocrystals; chapter 4 discusses emission and lifetime studies on rare earth doped GaN that comes in the form of a powder; and chapter 5 presents results on dye-rich core-shell silica nanoparticles.

CHAPTER 2
PHOTOLUMINESCENCE ENHANCEMENT AND INHIBITION
COLLOIDAL QUANTUM DOTS

2.1 Introduction

Semiconductor quantum dots (QDs), or nanocrystals, have sparked a tremendous amount of interest in both the research community and industry. These intensely fluorescent particles have a high absorption cross section compared to other visible fluorophores such as organic dyes [2, 3]. The size dependence of the optical and electronic properties of QDs render them promising materials for photonic applications such as organic-inorganic hybrid solar cells [4], white light lasers and energy converters [5–8], and tunable sources of infrared radiation [9].

This work focuses on colloidal nanocrystals (NCs). The NCs come in a liquid solution, usually consisting of a solvent as light as toluene or heavier like octane. This necessarily and obviously leads to an easy control of the surface density of the NCs when they are used to coat a substrate by a spin-on process for example. Another advantage of using NCs is that their surface can be easily chemically functionalized, allowing for their use in conjunction with various materials and in various environments. For a nice overview of such applications, see [10].

There have been several successful attempts to incorporate NCs into light controlling photonic structures. Examples include NCs embedded in microspheres [11–15]. Most demonstrations of enhancement and inhibition of spontaneous emission (at the time that we conducted the experiments) have relied on the construction of the photonic structure on the substrate of the active layer itself. This obviously limits such applications to specific sets of materials: one is limited to

materials that are compatible with the substrate. Examples include self-assembled QDs in photonic crystals [16,17], single QDs embedded in pillar microcavities [18], and epitaxially grown quantum wells in planar microcavities [19]. In the case of self-assembled QDs, the nature of the growth technique also makes it difficult to control the number of QDs interacting with the optical field.

The NCs that were used for our experiments were fabricated in the laboratories of Professor Todd D. Krauss at the University of Rochester. The CdSe NCs were synthesized in coordinating solvents using variations of methods previously published [20,21]. The core diameter of the NCs was 2.8 nm as determined from optical absorption spectroscopy. In order to passivate the outer surface of the (smaller bandgap) NCs, they were capped with a (larger bandgap) layer of ZnS according to literature methods [22,23]. This capping presents several advantages, namely to improve the luminescence of the NCs and to render the NCs more stable by protecting them from their surroundings.

The goal of our experiments was to show that control over the spontaneous emission of NCs was possible by demonstrating photoluminescence enhancement and inhibition [24,25]. The control of the emission properties of NCs is greatly desirable for several reasons. Enhancing or suppressing the photoluminescence can be desirable in order to control when the emitted light is to be made available. Spatial control over the luminescence of NCs is most desirable in order to direct this emission in certain directions. As is shown in the next sections, such control can be realized by controlling the photon density of modes.

Several techniques for the calculation of conduction and valence band states in NCs have been used. Examples include the pseudopotential approach by Zunger *et al.* [26–28], a tight binding method was also used to calculate the energy levels

of the NCs [29], and the effective mass approximation [30].

2.2 Photoluminescence Enhancement

In free space, excited NCs can photoluminesce in all directions, i.e. without any restrictions as to where this emitted radiation can go. In fact, it was recently shown that the radiation pattern of single CdSe NCs is that of three perpendicular dipoles [31]. The use of NCs for integrated (on-chip) applications therefore requires that their emission be controlled so that it can be used in an effective manner.

2.2.1 Density of Photon Modes

This section deals with the control of the emission properties of the NCs. In the present case, this is achieved using periodic photonic structures in one dimension (1D). Such structures are known to confine and enhance the electromagnetic field by orders of magnitude [32].

Fermi's Golden Rule dictates the spontaneous emission rate of an excited atom starting in its initial (excited) state and dropping into its final (relaxed) state by spontaneously emitting a photon of momentum $\hbar\mathbf{k}$ is given by

$$W_{Spont} = \frac{2\pi}{\hbar^2 c} \sum_{\mathbf{k}} |\langle \phi_f | e\mathbf{d} \cdot \mathbf{E} | \phi_i \rangle|^2 \rho(\mathbf{k}), \quad (2.1)$$

where ϕ_f and ϕ_i are the final and initial states, respectively, of the atom (or atom-photon) system, the matrix element $e\mathbf{d} \cdot \mathbf{E}$ is the manifestation of the interaction between the atom and the electromagnetic field (here, the electric dipole interaction is considered), and ρ is the mode density of the optical field at frequency $\omega = c|\mathbf{k}|$ in the \mathbf{k} direction. It is clear from equation 2.1 that the spontaneous emission rate

of an atom, or in our case a NC, can be affected by changing the density of modes ρ .

The work presented here shows control over the density of modes (DOM) in 1D by using a one dimensional microcavity formed between two distributed Bragg mirrors. Such a microcavity, which is essentially a Fabry-Pérot resonator, drastically alters the DOM into which the NCs can emit radiation. It is interesting to compare the DOM in free space to that of the Fabry-Pérot microcavity. Since the type of Fabry-Pérot resonator that is used here is 1D, let us compare the DOM in free space (in 1D) to that of the resonator.

In the case of a 1D (homogeneous) medium, the DOM is calculated by considering an electromagnetic wave confined in the 1D medium of length a . This wave, which must satisfy the boundary conditions in the 1D medium, follows the equation

$$E_l^0 \sin(k_l x), \quad (2.2)$$

where E_l^0 is the amplitude of the l^{th} optical mode. Then, since $k_l = l\pi/a$, each discrete mode in k -space is separated by a value π/a . Noting that there is 1 mode per interval π/a , this means that there will be N modes in an interval between 0 and, say, k_{max} . In other words,

$$N = \frac{k_{max}}{\pi/a} = \frac{2\pi n\nu/c}{\pi/a} = \frac{2n\nu a}{c}, \quad (2.3)$$

where n is the index of refraction of the medium. The final quantity of interest, the DOM in free (1D) space, in units of number of modes per unit frequency per unit length (of the medium), is given by

$$\rho(\nu) = \frac{1}{a} \frac{\partial N}{\partial \nu} = \frac{2n}{c}. \quad (2.4)$$

We now need to compare the DOM in 1D in "free space", equation 2.4, to the DOM in 1D for a confined system, i.e. for our planar microcavity.

In order to fabricate a dielectric 1D microcavity that will be suitable for the task at hand, computer simulations must be undertaken in order to determine the exact parameters of the structure, i.e. the thicknesses of all the layers that will comprise the distributed Bragg reflectors between which a microcavity will be formed. The results from these calculations give us the DOM that we are seeking.

The book by Hecht [33] gives an excellent description of how to calculate the reflection and transmission coefficients of multilayered films. These calculations are so fundamental, however, that it is worthwhile recalling the main steps. In keeping with the nomenclature of Hecht for simplicity, consider figure 2.1 which shows the electromagnetic fields of a linearly polarized light propagating across the boundaries of three thin films, with the central film of thickness d .

Each film which comprises a multilayered stack is assigned a characteristic matrix of the form

$$\mathcal{M} = \begin{pmatrix} \cos(k_0 h) & \frac{i}{Y_1} \sin(k_0 h) \\ Y_1 i \sin(k_0 h) & \cos(k_0 h) \end{pmatrix}, \quad (2.5)$$

where $k_0 h = k_0 n_1 d \cos(\theta_{IncII})$ and $Y_1 = \sqrt{\varepsilon_0/\mu_0} n_1 \cos(\theta_{IncII})$ for the case where \mathbf{E} is normal to the plane of incidence¹. For the case where \mathbf{E} is in the plane of incidence, then $Y_1 = \sqrt{\varepsilon_0/\mu_0} n_1 / \cos(\theta_{IncII})$. If there are p films in the multilayered stack, then the entirety of the stack is represented by the product of the

¹Figure 2.1 is actually a cross section in the plane of incidence. Therefore, the electric field components \mathbf{E} as drawn are perpendicular to the plane of incidence.

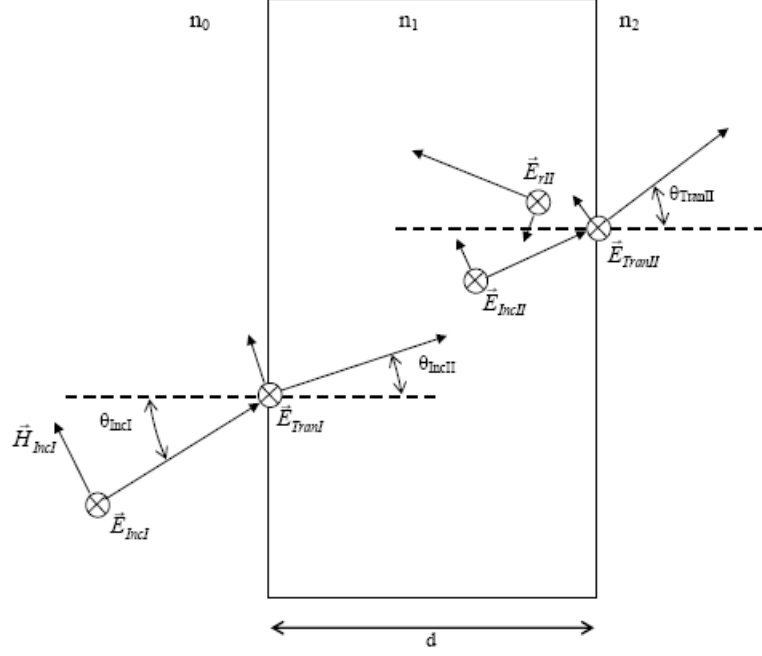


Figure 2.1. Electromagnetic fields of a linearly polarized wave propagating across the boundaries between three thin films.

characteristic matrix \mathcal{M} . The resulting matrix can then be written as

$$\mathcal{M} = \mathcal{M}_I \mathcal{M}_{II} \mathcal{M}_{III} \dots \mathcal{M}_p = \begin{pmatrix} m_{11} & m_{12} \\ m_{21} & m_{22} \end{pmatrix}. \quad (2.6)$$

Noting that each characteristic matrix relates the incident and transmitted electromagnetic fields at the boundaries of its corresponding film, it is now possible to obtain the reflection and transmission coefficients from the final characteristic matrix in equation 2.6. The results are given by

$$r = \frac{Y_0 m_{11} + Y_0 Y_s m_{12} - m_{21} - Y_s m_{22}}{Y_0 m_{11} + Y_0 Y_s m_{12} + m_{21} + Y_s m_{22}}, \quad \text{and} \quad (2.7)$$

$$t = \frac{2Y_0}{Y_0 m_{11} + Y_0 Y_s m_{12} + m_{21} + Y_s m_{22}}, \quad (2.8)$$

where now $Y_0 = \sqrt{\varepsilon_0/\mu_0} n_0 \cos(\theta_{Incl})$, and $Y_s = \sqrt{\varepsilon_0/\mu_0} n_s \cos(\theta_{TranII})$, with the

subscript s representing the last film in the stack.

Equations 2.7 and 2.8 now allow us to calculate the reflection and transmission spectra, hence the DOM, of our 1D microcavity formed between two DBRs. For example, the reflection spectrum (i.e. the power reflection coefficient) will be given by $R = rr^*$. Another useful calculation which can be derived from the transfer matrix method is the electric field distribution throughout a given stack. Indeed, the resulting matrix for a given stack, as described by equation 2.6, relates the electric and magnetic fields E_0 and H_0 that are incident onto the stack to the electric and magnetic fields E_n and H_n that are exiting the stack via

$$\begin{pmatrix} E_0 \\ Y_0 H_0 \end{pmatrix} = \mathcal{M} \begin{pmatrix} E_n \\ Y_s H_n \end{pmatrix}. \quad (2.9)$$

A few calculations reveal that

$$\begin{pmatrix} 1 + r \\ Y_0(1 - r) \end{pmatrix} = \mathcal{M} \begin{pmatrix} E_n \\ Y_s H_n \end{pmatrix}. \quad (2.10)$$

Now, \mathcal{M} has an inverse since

$$\begin{aligned} \det(\mathcal{M}) &= \det(\mathcal{M}_I \mathcal{M}_{II} \mathcal{M}_{III} \dots \mathcal{M}_p) \\ &= \det(\mathcal{M}_I) \det(\mathcal{M}_{II}) \det(\mathcal{M}_{III}) \dots \det(\mathcal{M}_p) \\ &= 1, \end{aligned} \quad (2.11)$$

because the determinant of a transfer matrix \mathcal{M} for any film is unity, which satisfies the necessary and sufficient condition for an inverse of a matrix to exist.² This therefore means that the electric (and magnetic) field inside and throughout any i^{th} film can be calculated using

$$\mathcal{M}_{0 \rightarrow i}^{-1} \begin{pmatrix} 1 + r \\ Y_0(1 - r) \end{pmatrix} = \begin{pmatrix} E_i \\ Y_i H_i \end{pmatrix}. \quad (2.12)$$

²A matrix \mathbf{A} will have an inverse *if and only if* $\det \mathbf{A} \neq 0$.

As a direct application of equation 2.12, it is instructive to visualize how the electric field (or $|E|^2$) is distributed throughout a low index microcavity formed between two DBRs. Figure 2.2 below shows (qualitatively) the distribution of the intensity ($|E|^2$) throughout a structure consisting of a $\lambda/2n$ microcavity formed between two DBRs of six pairs of $\lambda/4n$ layers of alternating indices of refraction. The intensity is strongest at the center of the device, which suggests that the active material should be placed as close as possible to that region inside the microcavity. If the microcavity had a thickness of $3\lambda/2n$, there would be two (longitudinal) modes throughout the device, and two equal peaks of equal intensity would be observed inside the microcavity as opposed to a single peak.

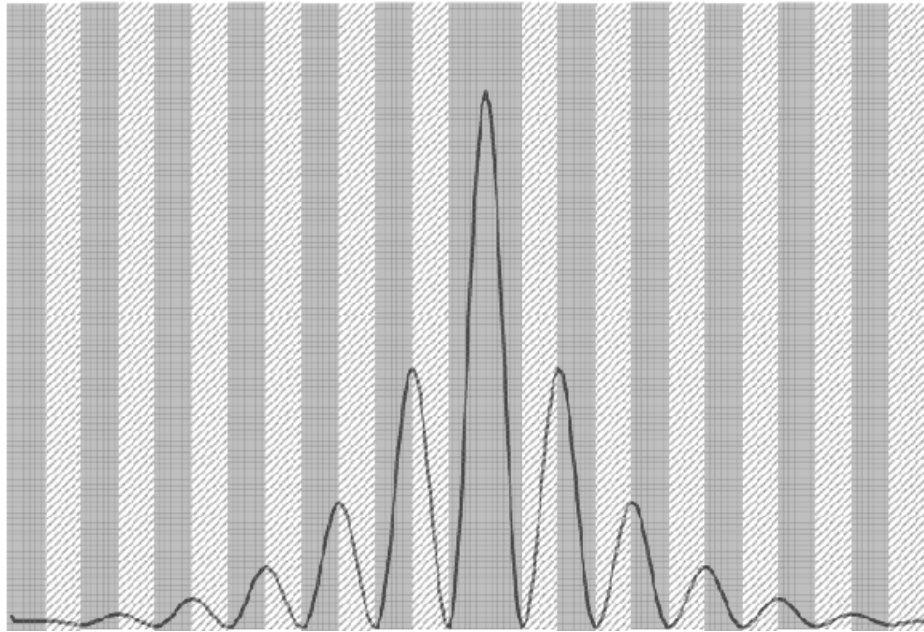


Figure 2.2. Intensity ($|E|^2$) of the field throughout a microcavity with six pairs of $\lambda/4n$ layers of alternating indices of refraction with a $\lambda/2n$ microcavity. The light grey regions represent a material with higher index of refraction than the dark grey regions.

Before calculating the transmission of the microcavity, it is instructive to start with the calculation of the reflection spectrum of a DBR made of quarter wavelength thick slabs, i.e. each slab having a thickness of $\lambda_0/4n$, where λ_0 is the wavelength about which the reflectivity of the DBR will be highest.

Consider the case where six pairs (in anticipation of section 2.2.2) of dielectric layers are stacked on a glass substrate ($n = 1.46$), where each layer in a pair has a high and low index of refraction ($n_H = 2.1$ and $n_L = 1.46$). Figure 2.3(a) shows the calculated transmission spectrum of this (lossless) stack, where each layer measures $\lambda_0/4n$ with $\lambda_0 = 552.7$ nm, again in anticipation of the following section. The figure shows a distinct decrease in transmission (or increase in reflection) at and about λ_0 . Now, if a microcavity is formed between two DBRs whose spectra are as that of figure 2.3(a), the result is as shown in figure 2.3(b) where a resonance appears exactly at λ_0 . In this case, a layer of thickness $\lambda_0/2n_L$ exists between the two six-layer DBR stacks.

Figure 2.3(b) shows the sharp contrast between the DOM that was calculated in equation 2.4, which is qualitatively shown as the dotted line (and whose position on the graph does not correspond to the transmission abscissa but is merely plotted as a visual aid). The effect of the microcavity is to alter the density of modes from a constant value that an emitter sees in free space (equation 2.4) to allowed emission only at certain wavelengths (or frequencies) with a definite weight which is determined by the microcavity. It is by this alteration of the DOM via the microcavity that the spontaneous emission rate for the emitter, equation 2.1, can be altered.

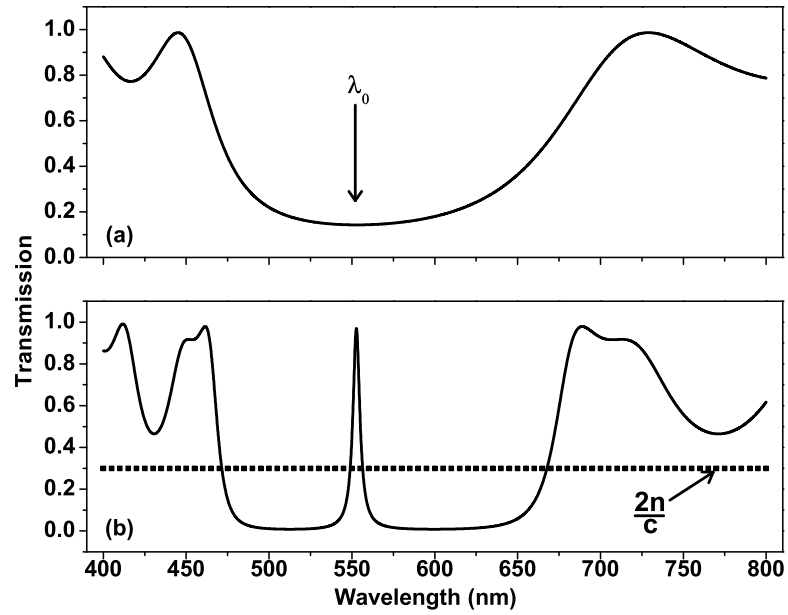


Figure 2.3. Calculated transmission spectra, for $\lambda_0 = 552.7$ nm, of stacks of quarter wavelength ($\lambda_0/4n$) films of alternating indices of refraction ($n_H = 2.1$ and $n_L = 1.46$) in the case of (a), a six pair DBR of n_H - n_L layers; and (b), a $\lambda_0/2n_L$ microcavity formed between two DBRs with reflection spectra as shown in (a). The dotted line represents qualitatively the DOM in 1D free space.

2.2.2 Experiment and Results

Using the tools derived in the previous section, a microcavity can be tailored to have its resonance at the emission peak of the NCs in order to show photoluminescence enhancement.

The CdSe NCs that were used in the experiment had a free space photoluminescence spectrum as shown in figure 2.4. The 457.9 nm line of an argon laser was used to excite the NCs at an intensity of 0.14 W/cm^2 . The same (standard) optical setup was used for all photoluminescence measurements in this experiment. It consisted of a first lens to collimate the emission from the sample and a second lens to focus the collimated beam onto the monochromator's input slit. The second lens's focal length (more precisely its $f\#$) is such that it is equal or less than the monochromator's $f\#$, the latter being. The output of the monochromator was equipped with a Hamamatsu photomultiplier tube 1P28. The peak emission wavelength of the NCs is at $\lambda_0 = 552.7 \text{ nm}$.

The microcavity was fabricated in the Cornell NanoScale Science and Technology Facility (CNF). The materials of interest, i.e. materials that present good optical properties in the wavelength range of interest (low absorption and high index contrast), that were used for the DBR layers were SiO_2 and TiO_2 . Sputtering (CVC Magnetron Sputter system) was used to deposit the thin films. The SiO_2 films were deposited using an SiO_2 target of 99.99% purity in an argon ambient under a pressure of 4 mTorr. 1.5 kW of RF power was used. The deposition rate of the SiO_2 films was of 5 nm/min. The TiO_2 films were deposited using a Ti target of 99.99% purity in an oxygen ambient under a pressure of 5 mTorr. 2 kW of DC power was used. The deposition rate of the TiO_2 films was of 1 nm/min. The deposition rates were determined (and confirmed) in two ways, by ellipsome-

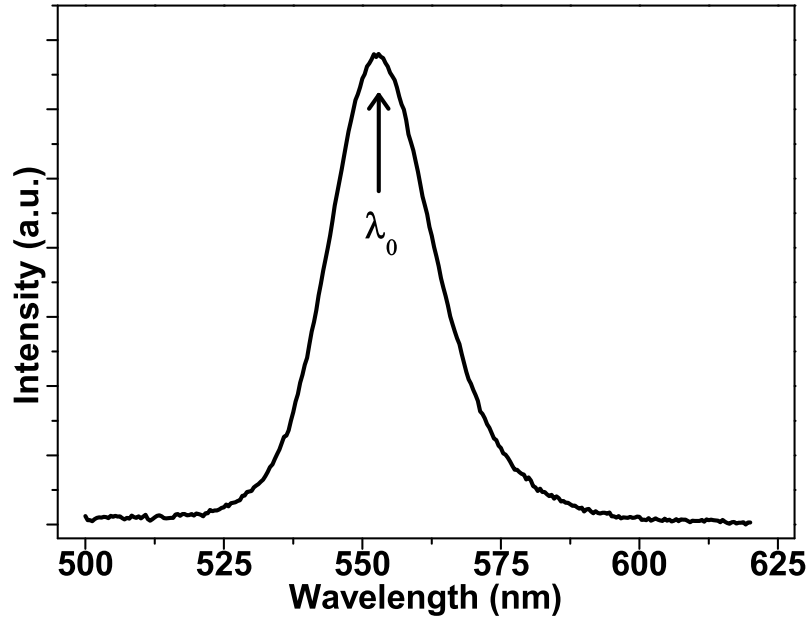


Figure 2.4. Free space photoluminescence of the CdSe NCs used in the experiment under the 457.9 nm laser line of an argon laser.

try and by physical measurement. While ellipsometry was performed using CNF equipment, physical measurements of the thickness of the deposited layers was evaluated by doing a test run for a given amount of time on a witness sample consisting of a small ($\sim 1 \text{ cm} \times 1 \text{ cm}$) piece of silicon on which lines of photoresist were "drawn". The photoresist was removed (using acetone under sonication) from the sample after the layer deposition and a measurement of the thickness of the layer was performed using a profilometer like the Tencor P10. This thickness is obtained from the difference in height between the substrate (Si) and the film. The deposition rate is then calculated (film thickness divided by deposition time).

The indices of refraction of the materials were determined by ellipsometry. The index of SiO_2 was determined to be $n_L = 1.46$ after a test run of 30 minutes, and

the index of TiO_2 was determined to be $n_H = 2.3$ after a test run of 30 minutes. These are the values that were used to determine the required thickness of the layers involved in the DBRs.

A distinct advantage of the sputtering system that was used is the fact that variations in the thickness of the film layers are possible. The CVC system consists of a large circular platter (the rotostrate) on which the samples are placed, and which rotates under the sputtering targets. The layer deposition in the chamber is such that the thickness of the layers varies uniformly, from thinner to thicker, as a function of the radial distance (i.e. the distance from the center of the rotostrate). This therefore allows for the formation of DBRs that are "tunable" in the sense that their frequency response will depend on the position where the measurements are made on the sample.

The fabrication process for the entire structure went as follows. A microscope glass slide was subjected to an oxygen plasma. The purpose of the oxygen plasma was to remove any organic material on the surface of the glass slide. The Glen 1000P Plasma Cleaning System was used for five minutes in an oxygen ambient at 42 standard cubic centimeters (SCCM) of O_2 flow and 400 Watts of power. Six pairs of high index (TiO_2) and low index (SiO_2) thin films were then deposited in the sputtering system. The target thickness of all but the last SiO_2 layer was $\lambda_0/(4 \times 1.46) = 94.6$ nm, and the target thickness of the TiO_2 films was $\lambda_0/(4 \times 2.3) = 60.1$ nm. The last layer of SiO_2 , which formed the first half of the $\lambda/2n$ microcavity, had to be thinner in order to account for the thickness of the NCs. The durations of the depositions of the SiO_2 and TiO_2 films were therefore 18.9 and 60.1 minutes respectively. The NCs were then spin coated onto the sample to form a thin layer. The spin coating process was effected at 2000 RPM for 60

seconds. Ellipsometric measurements on previously spin coated microscope slides revealed a thickness of about 95 nm for the NCs with an index of about 2.8. Note that these values were obtained from an average of several measurements. The rest of the DBR layers were then deposited on the sample, starting with SiO₂, which formed the second half of the microcavity, followed by the other layers.

A reference sample was also needed in order to compare the effect of the microcavity on the photoluminescence to the free space photoluminescence. NCs were therefore spin coated onto a cleaned microscope slide (see previous paragraph) and coated with a 75 nm layer of sputtered SiO₂.

The maximum temperature on the rotostrate was determined to be about 140 C. A non-reversible Omegalabel temperature label was affixed under a silicon wafer which rests on the rotostrate. It was found that this temperature, even maintained for several hours, was not detrimental to the (CW) photoluminescence characteristics of the NCs. It is possible that the initial high vacuum in the sputtering chamber (before the gases necessary for the sputtering are pumped into the chamber), on the order of 10⁻⁷ Torrs, combined with the fact that the first gas to which the NCs are exposed is argon, a noble gas, prevent the NCs from oxidizing (see for example [34]).

Figure 2.5 below shows a schematic representation of the finished structure. The 3D schematic shows the wedged aspect of the structure, where the thickness of the sputtered films is thicker in certain regions and thinner in others. The top portion of the figure shows two measured transmittance spectra on regions on the sample where the films are thicker (top spectrum) and thinner (bottom spectrum). The clear effect of the variations of the film thicknesses is evident in the shift of the position of the microcavity's resonance. Note that the variation in the thickness of

the films is smooth and continuous, and that therefore the corresponding spectra show resonances which vary accordingly.

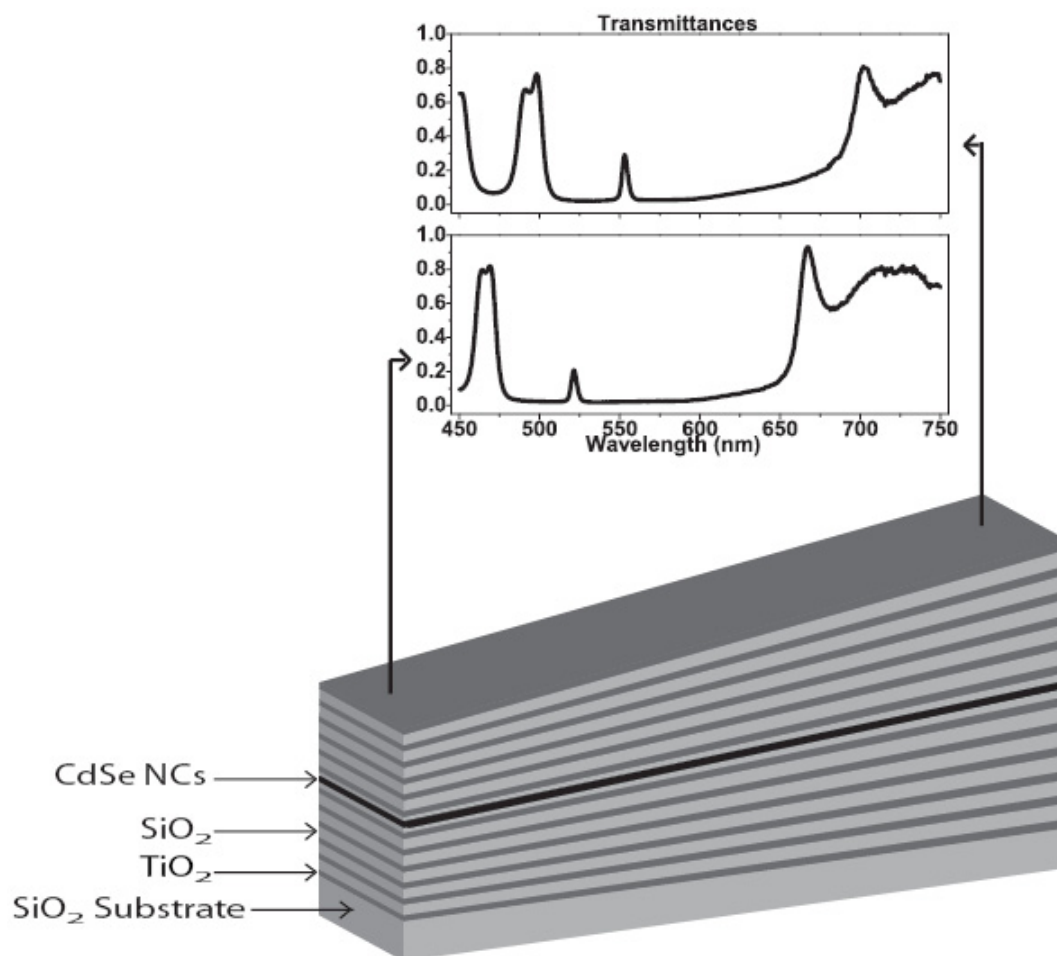


Figure 2.5. 3D schematic representation of the final structure, with its wedged characteristic. Thicker film regions have a correspondingly higher wavelength resonance (top spectrum), while thinner film regions have a lower wavelength resonance (bottom spectrum).

The transmittance spectra were obtained with a conventional setup, where a white light source (halogen bulb) is collimated and an aperture (of about 1 mm in diameter) limits the amount of light impinging onto the sample. This spectrum (the transmission spectrum) is normalized to the white light's spectrum to obtain

the transmittance. A lock-in amplifier system was used for all photoluminescence (not lifetime) and reflection/transmission measurements. An optical chopper set at a chopping frequency of a few hundred Hertz results in good measurements, where the chopper is inserted in the optical path of the excitation (i.e. the white light source for reflection/transmission measurements, or the laser in the case of photoluminescence measurements).

In order to measure the effect of the microcavity on the photoluminescence of the NCs, the spectrum of the emission of the NCs from the microcavity was measured and compared to the spectrum of the NCs in the reference spectrum. In order to show enhancement of the photoluminescence, the microcavity's resonance has to be the same as the NCs emission peak, i.e. 552.7 nm. Figure 2.6 below shows the transmission spectrum of the microcavity (solid line) with its resonance matching exactly that of the emission peak of the NCs (dashed line). The microcavity's resonance has a full width at half maximum (FWHM) of 4.1 nm, and its corresponding quality factor (Q) is $\lambda/\Delta\lambda = 135$. The FWHM of the photoluminescence of the NCs in free space is 22.1 nm. From figure 2.6, it is clear that the microcavity's resonance does not reach (near) unity as predicted by the theoretical calculations (see figure 2.3(b)). This is caused by absorption. In fact, as was reported in [24], the absorption of the NCs at the emission wavelength is enhanced due to the cavity effect. The magnitude of this absorption enhancement was obtained by fitting calculated transmission spectra to the measured spectra for different cavity resonances using the transfer matrix method as described on page 7. From the curve fits of the theoretical spectra and the experimental transmission spectra (for resonances between 530 nm and 580 nm), the cavity thickness and the NCs layer extinction ratio as a function of wavelength were determined. This re-

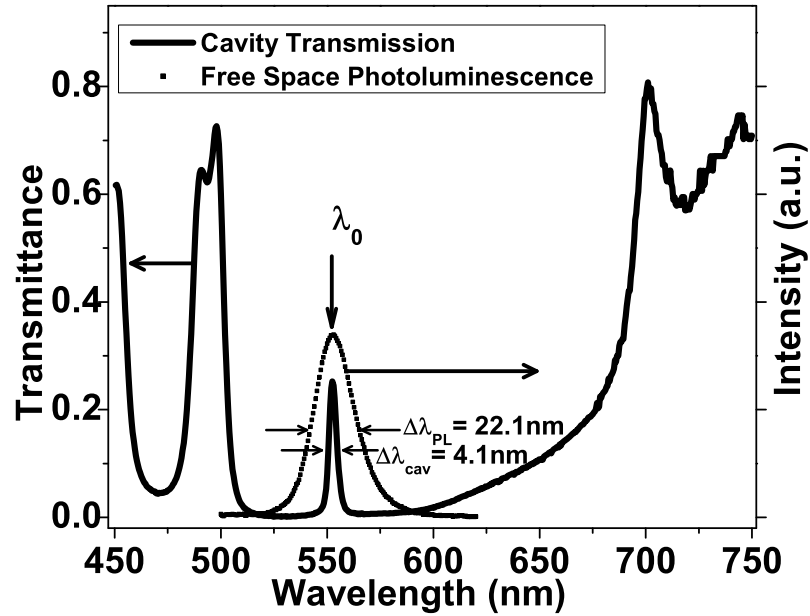


Figure 2.6. Measured transmission of the monolithic Fabry-Pérot microcavity embedded with NCs. Superimposed is the free space photoluminescence spectrum of the reference sample.

sulted in using indices of refraction of 1.46 and 2.1 for SiO₂ and TiO₂ respectively. It is worth noting that the value for the index of refraction for TiO₂ is slightly different than the previous value measured by ellipsometry (2.3) on page 14. The reason for this is attributed to the fact that since the deposition time for the thin films is of several hours (about 18 hours total for the entire structure), residual, unreacted O₂ remains in the sputtering chamber between the reactive Ti + O₂ runs, resulting in oxygen rich TiO₂ (Ti_xO_y) films with a lower index of refraction.

Figure 2.7(a) below shows the transmission spectra of three cavity resonances along with the fitted theoretical data. In figure 2.7(b), the absorption obtained from the fitted spectra is shown together with the absorption of the reference

sample. The absorption at the emission wavelength is amplified by an order of magnitude. Similar effects have been previously shown (see for example [35] for the enhancement for absorption in the case of embedded quantum wells in microcavities). This is attributed to the light confinement in the microcavity. In the case of NCs, this effect is especially strong due to the fact their free space absorption is significant at and near the emission wavelength. This significant enhancement of the absorption does limit the effective Q that can be achieved since the electric field in a strongly absorbing system is weaker compared to a system with less absorption. This limitation on the Q is therefore important in systems when the emission linewidth approached that of the cavity linewidth, where the coupling to the cavity is strongly dependent on the cavity Q . Figure 2.8 shows the photoluminescence spectra measured at two different positions on the sample, with these positions corresponding to microcavities in and out (dotted and dashed lines, respectively) of resonance with the free space emission peak of the NCs, 552.7 nm. For comparison, the photoluminescence spectrum of the reference sample is shown on the same scale. It is clear from the figure that the cavity has an enhancement effect on the photoluminescence of the NCs. The spectrally integrated photoluminescence from the cavity structure which is in resonance with the emission peak wavelength of the free space emission is enhanced by a factor of 2.7 ± 0.6 compared to the integrated photoluminescence of the reference sample. The FWHM of the NCs emission is also considerably narrowed from a free space value of 22.1 nm to 6.6 nm. The spectra in figure 2.8 also show a background which corresponds to the photoluminescence spectrum of the NCs in free space. These emissions which do not correspond to the cavity resonance indicates that some of the NCs are not exclusively in the microcavity. It is possible that, as a

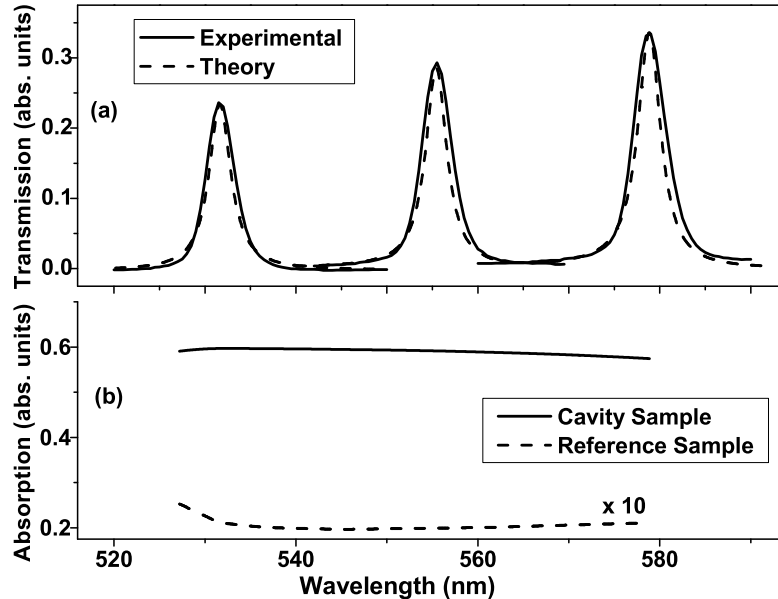


Figure 2.7. (a) Experimental and theoretical transmission spectra for three different cavity resonances. (b) Calculated absorption of the cavity and reference samples as a function of wavelength.

result of the sputtering process, some of the NCs may end up being embedded in the top DBR. We can compare the experimental photoluminescence enhancement to the theoretical value. Indeed, in a 1D microcavity, the integrated photoluminescence enhancement (perpendicular to the lay plane of the layers) can be calculated using [36]

$$\frac{\Gamma}{\Gamma_0} = \frac{2F}{\sqrt{2\pi}} \xi, \quad (2.13)$$

where $\xi = |E_{dots}|^2 / |E_{max}|^2$ represents the effective intensity of the electric field at the NCs layer relative to the peak value of that electric field intensity in the cavity region. The finesse F is given by $\lambda_0 Q / 2nd$. However, when calculating the finesse F , when $\Delta\lambda_{PL} \gg \Delta\lambda_{cav}$, which can be assumed is the case here (see figure 2.6), the

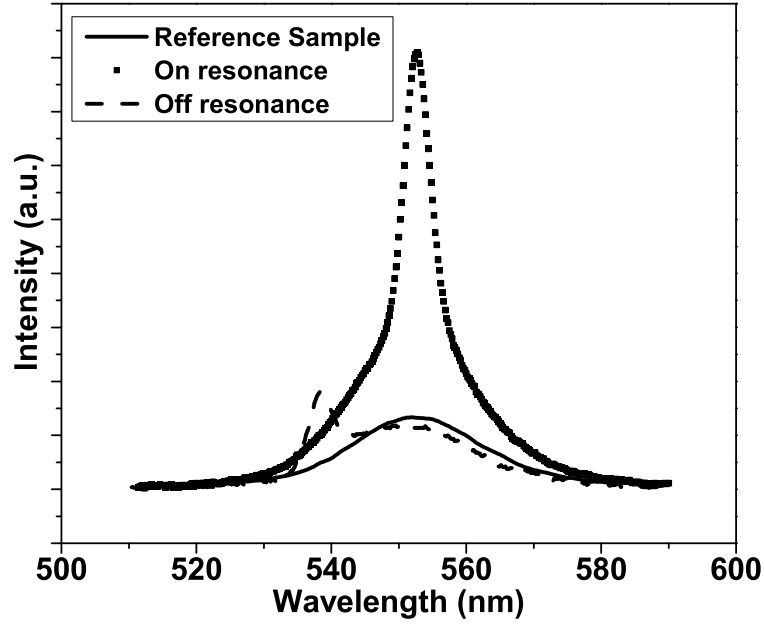


Figure 2.8. Photoluminescence of the NCs from within the microcavity on and off resonance (dotted and dashed lines respectively) with the emission peak of the NCs in the reference sample (solid line).

Q that must be used [37] is that of the emitting material, i.e. $Q = \lambda_0/\Delta\lambda_{PL} = 25$. From this, $F = 27.6$. Lastly, ξ is evaluated using the transfer matrix method as previously described on page 7, more precisely equation 2.12. A value of $\xi = 0.34$ was obtained. This leads to a value for the enhancement of $\Gamma/\Gamma_0 = 4.5$. The small discrepancy between the theoretical value for the photoluminescence enhancement of 4.5 and the experimental value of 2.7 ± 0.6 is attributed to inhomogeneities in the spin-coated NC layer.

Another interesting effect that can be observed is the shift to higher energy (shorter wavelength) of the position of the cavity's resonance as a function of the collection angle, this angle being measured with respect to the normal to the surface

of the sample. Figure 2.9 shows this change in the cavity's resonance as a function of the collection angle. The inset in the figure shows how the angle θ is measured with respect to the sample's surface. Note that the inset, which is a scaled down version of figure 2.5, shows a greatly exaggerated difference in the wedge aspect of the structure. The change of the cavity's resonance is approximately 4nm for every mm change in the position where the emission is collected on the sample. Effectively, this results in a slope in the films of the structure of less than 2×10^{-5} .

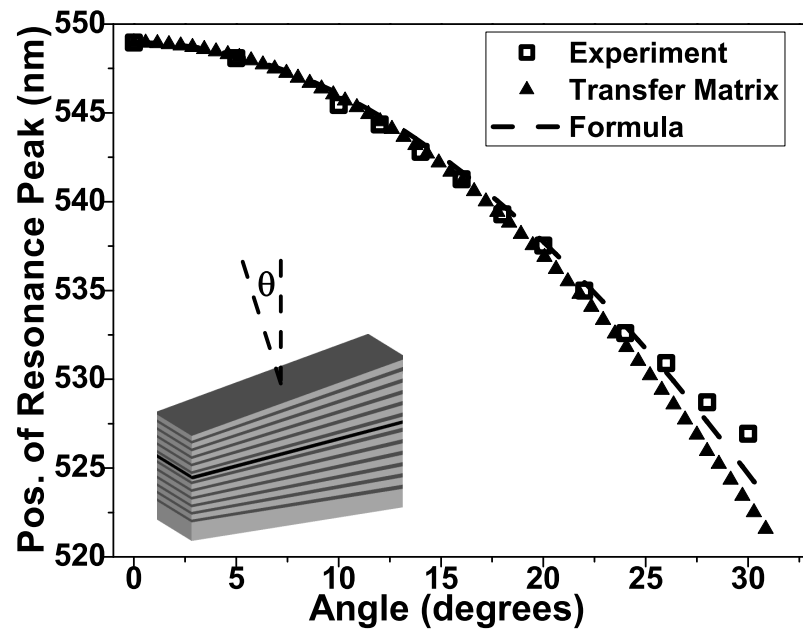


Figure 2.9. Position of the cavity's resonance as a function of the collection angle θ . The square symbols represent the experimental measurements, while the other two are theoretical: the triangles represent the transfer matrix method simulations, and the dashed line the formula derived below (see equation 2.18). The inset shows how the angle θ is measured with respect to the sample.

Also shown in figure 2.9 are the theoretical calculations of the position of the

cavity's resonance. The triangles in the figure are obtained from the transfer matrix method as described on page 7. The dashed line in figure 2.9 is obtained by a somewhat more intuitive and simple calculation. For its derivation, consider figure 2.10 which is a simplified version of the microcavity confined between two DBRs. The resonance condition, at normal incidence (i.e. for $\theta = \theta_{cav} = 0$) is given by

$$2k_0 n_{cav} d = m2\pi = \frac{4\pi n_{cav} d}{\lambda_0} \Rightarrow \lambda_0 = \frac{2n_{cav} d}{m}, \quad (2.14)$$

where m is an integer. For light propagating at a given angle θ_{cav} from the cavity, the resonance condition is then given by

$$2k_1 n_{cav} d \cos \theta_{cav} = m2\pi = \frac{4\pi n_{cav} d \cos \theta_{cav}}{\lambda_0} \Rightarrow \lambda_1 = \frac{2n_{cav} d \cos \theta_{cav}}{m}. \quad (2.15)$$

The last two equations can be combined to give

$$\lambda_1 = \lambda_0 \cos \theta_{cav}. \quad (2.16)$$

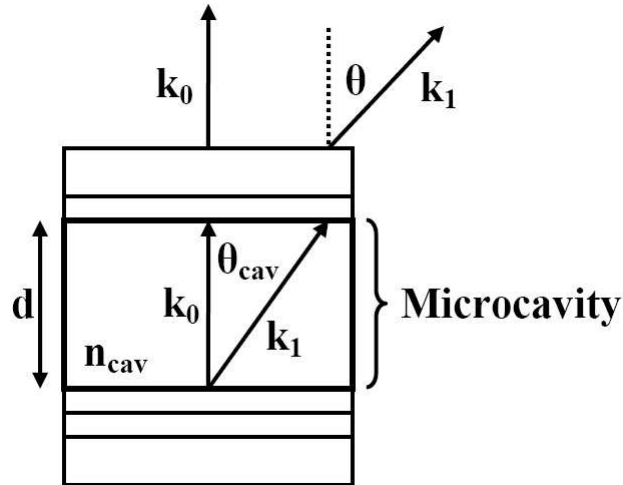


Figure 2.10. Simple schematic for the calculation of the blue shift of the cavity's resonance as a function of the collection angle θ .

The equation that relates the angle θ_{cav} to the angle at which the measurement is taken outside the cavity θ_{air} is obtained by using Snell's law

$$\theta_{cav} = \sin^{-1} \left(\frac{\sin \theta_{air}}{n_{cav}} \right). \quad (2.17)$$

Finally, combining now the last two equations, we get

$$\lambda_1 = \lambda_0 \cos \left(\sin^{-1} \left(\frac{\sin \theta_{air}}{n_{cav}} \right) \right). \quad (2.18)$$

Both the transfer matrix method and the formula of equation 2.18 give excellent agreement with the experimental results as shown in figure 2.9. It does appear that at higher collection angles the experimental curve does not show a cavity peak moving as quickly with an increasing collection angle. This is due to the experimental setup which was used to measure the emission. Although objective lenses were used both for the excitation (to focus the Ar laser to a small spot) and the collection (to acquire a small solid angle of the emission), the collection of the emission is such that an averaging over its solid angle collection occurs, which affects the results more greatly at higher angles since the emission becomes weaker. The result of this is as seen in the experimental curve in figure 2.9 where, at higher angles, the position of the resonance peak does not shift as steeply to shorter wavelengths as the theoretical curves.

A quick note with regard to the longevity of the CdSe NCs that were used is worthwhile. The sample used for the experiments herein described was fabricated in August 2002, and the measurements as shown in figures 2.5, 2.6, 2.7 and 2.8 were performed within the following few months. The results discussed in the previous three pages with regard to the angle measurements were performed in April 2006. The emission CdSe photoluminescence from the almost 4 year old sample, which was stored at room temperature in ambient air in a non-hermetic, opaque but not

light blocking plastic microscope slide holder (of the UniMailer type as sold from Ted Pella), appeared to remain bright and stable.

The fact that the photoluminescence of the embedded NCs is enhanced is indicative that there is coupling of the NCs to the cavity mode. What is particular to this case is that it is coupling of a colloidal NC system. This therefore allows for the possibility of endowing light properties to optically inactive systems. This sort of coupling permits control over the intensity and lifetime of NCs. For example, modification of light emission and radiative lifetime has been shown for CdSe NCs in hollow microspheres [38]. Recently, cavity quantum electrodynamic effects of strong coupling between a CdSe NC (a CdSe nanorod was in fact used, with minor and major axes of 2.5 nm and 25 nm respectively) and a polymer microsphere has been shown [39].

CHAPTER 3
FÖRSTER ENERGY TRANSFER IN COLLOIDAL QUANTUM
DOTS

3.1 Introduction

The process of Förster resonant energy transfer (FRET) involves a donor D (atom, molecule, etc.) and an acceptor A (atom, molecule, etc.), where the emission spectrum of the donor overlaps with the absorption spectrum of the acceptor. An excited donor can transfer its energy resonantly to a non-excited acceptor. This results in the donor losing its energy and going into a relaxed state, and the acceptor going from a relaxed state to an excited state.

Such a process is indeed important and has promising applications for devices. In nature, it has a key role in photosynthesis [40,41]. With regard to organic light emitting diodes for example, it can enhance the efficiency of the emission [42,43]. Taking advantage of FRET allows for the possibility of exciting a donor at a given (available to the user) wavelength and having the acceptor, which will be emitting at a different wavelength than the excitation wavelength available to the user, emit at another wavelength. The latter can be relatively distant from the excitation wavelength.

Nonradiative energy transfer (i.e. FRET) using semiconductor quantum dots has been previously shown in nanocrystal assemblies (close packed quantum dot solids) [44] and in an organic dye - CdSe quantum dots bilayer inside a microcavity [45]. Applications of systems that take advantage of FRET include biological sensing [46] and nanophotonics [47].

The work here involves studies of FRET of NCs placed in a 1D Fabry-Pérot

microcavity. The next section deals with the theoretical description of FRET. Section 3.3 discusses the experiment that was undertaken, with fabrication details and measurements. The effect of the microcavity is to prevent the donor from emitting radiation into its surrounding, thus enhancing the energy transfer to the acceptor which will be emitting into the resonant mode of the microcavity.

3.2 Quantum Electrodynamic Description of Förster Resonant Energy Transfer

Förster elegantly predicted the process of resonant energy transfer in 1948 [48]. The rate of transfer of energy between a donor D and an acceptor A separated by a distance r is given by [49]

$$k_T(r) = \frac{Q_D \kappa^2}{\tau_D r^6} \left(\frac{9000 \ln 10}{128 \pi^5 N n^4} \right) \int_0^\infty F_D(\lambda) \varepsilon_A(\lambda) \lambda^4 d\lambda, \quad (3.1)$$

where Q_D is the quantum yield of the donor in the absence of the acceptor, κ^2 describes the relative orientation in space of the transition dipoles of the donor and the acceptor (usually assumed to be 2/3 for dynamic random averaging of the donor and the acceptor), τ_D is the lifetime of the donor in the absence of the acceptor, N is Avogadro's number, n is the index of refraction of the medium, $F_D(\lambda)$ is the corrected fluorescence intensity of the donor (with the total intensity, i.e. the area under the curve, normalized to unity), and $\varepsilon_A(\lambda)$ is the extinction coefficient of the acceptor.

It is however more useful to rewrite equation 3.1 in terms of the Förster distance R_0 at which the transfer rate $k_T(r)$ is equal to the decay rate $1/\tau_D$:

$$R_0^6 = \frac{9000 \ln 10 Q_D \kappa^2}{128 \pi^5 N n^4} \int_0^\infty F_D(\lambda) \varepsilon_A(\lambda) \lambda^4 d\lambda. \quad (3.2)$$

Given the value for R_0 , the rate of energy transfer can be easily calculated using

$$k_T(r) = \frac{1}{\tau_D} \left(\frac{R_0}{r} \right)^6. \quad (3.3)$$

The transfer rate k_T can be compared to the decay rate of the donor $1/\tau_D$ to determine whether the transfer of energy is efficient ($k_T > 1/\tau_D$) or not ($k_T < 1/\tau_D$). The latter case simply means that little transfer of energy will occur (via FRET) during the lifetime of the excited state.

Lastly, the efficiency E of the transfer of energy can be calculated, which is simply the fraction of absorbed photons by the donor which are transferred to the acceptor,

$$E \equiv \frac{k_T}{\tau_d^{-1} + k_T} = \frac{R_0^6}{R_0^6 + r^6} = 1 - \frac{\tau_{DA}}{\tau_D}, \quad (3.4)$$

where τ_{DA} is the lifetime of the donor in the presence of the acceptor. Clearly, from equation 3.4, the higher the efficiency ($0 \leq E \leq 1$), the less the emission from the donor is observable as the donor's energy is efficiently transferred to the acceptor.

Quantum electrodynamics (QED) provides an excellent framework for the understanding and description of FRET. Not only does it actually give a designation to "real" and "virtual" photons, appropriate calculations, as shown below, actually provide the same result, i.e. the R^{-6} dependence of the energy transfer rate. The following QED derivations are the result of a summarization of several articles that have been published to date on the subject [50–57]. Some notations used in the following are in fact similar to and sometimes exactly like that used in some of those references. /clearpage FRET is a (electric) dipole-dipole (E1-E1) coupling,¹

¹This notation is standard, where E1 represents the electric dipole, E2 the electric quadrupole, M1 the magnetic dipole, M2 the magnetic quadrupole, etc.

i.e. it is dipole transitions in both the donor and acceptor that are involved in the exchange of energy. While an energy transfer via the magnetic dipole (E1-M1) is possible and is directly obtainable via QED (see for example [55]), it will not be considered here, although it can become the main transfer mechanism where the donor (or the acceptor) has an electric dipole transition which is not allowed [58]. Examples of where E1-M1 transitions exist involve, for example, lanthanide (terbium and europium) chelates where some spectral lines are attributed to magnetic dipole transitions.

The Hamiltonian of our system consisting of NCs each labeled σ , can be written as

$$H = \sum_{\sigma} H_{material}(\sigma) + \sum_{\sigma} H_{interaction}(\sigma) + H_{radiation}, \quad (3.5)$$

where $H_{material}$ and $H_{radiation}$ are the Hamiltonians for the material and radiation field respectively, and $H_{interaction}$ is the interaction Hamiltonian of the electric field with atom σ . This Hamiltonian H is exact. In our current electric dipole approximation, we can write $H_{interaction}$ as

$$H_{interaction}(\sigma) = - \sum_{\sigma} \boldsymbol{\mu}(\sigma) \cdot \boldsymbol{\mathcal{E}}_{\perp}(\mathbf{r}_{\sigma}). \quad (3.6)$$

It is clear that in the previous equation, the electric dipole operator $\boldsymbol{\mu}(\sigma)$ acts on the material states $|mat_n\rangle$ (it is, after all, a property of the material), and the transverse electric field operator $\boldsymbol{\mathcal{E}}_{\perp}(\mathbf{r}_{\sigma})$ acts on the radiation field states $|rad_n\rangle$, where the subscript n denotes the n^{th} eigenstate of the basis Hamiltonian as defined in equation 3.5 without the interaction term H_{int} . In other words,

$$|n\rangle = |mat_n\rangle |rad_n\rangle = |mat_n; rad_n\rangle. \quad (3.7)$$

In this last equation, $|mat_n\rangle$ is essentially a product of state vectors for each atom (molecule or, in our case, NC), and $|rad_n\rangle$ is the radiation (number or Fock) state.

It is well known that the transverse electric field operator $\mathcal{E}_\perp(\mathbf{r}_\sigma)$ can be written as, in our QED scheme (see for example [59]),

$$\mathcal{E}_\perp(\mathbf{r}_\sigma) = i \sum_{\mathbf{p}, \lambda} \left(\frac{\hbar c p}{2\epsilon_0 V} \right) \left\{ \boldsymbol{\mathcal{E}}^{(\lambda)}(\mathbf{p}) a^{(\lambda)}(\mathbf{p}) e^{i(\mathbf{p} \cdot \mathbf{r}_\sigma)} - \boldsymbol{\mathcal{E}}^{*(\lambda)}(\mathbf{p}) a^{\dagger(\lambda)}(\mathbf{p}) e^{-i(\mathbf{p} \cdot \mathbf{r}_\sigma)} \right\}, \quad (3.8)$$

where $\boldsymbol{\mathcal{E}}^{(\lambda)}(\mathbf{p})$ is the usual polarization unit vector, V is an arbitrary quantization volume, and $a^{(\lambda)}(\mathbf{p})$ and $a^{\dagger(\lambda)}(\mathbf{p})$ are the usual annihilation and creation operators, respectively, for a given mode identified by its momentum \mathbf{p} and polarization λ . The raising and lowering operators have the usual effect on the (radiation) states

$$a^{(\lambda)}(\mathbf{p}) |m(\mathbf{p}, \lambda)\rangle = \sqrt{m} |(m-1)(\mathbf{p}, \lambda)\rangle \quad (3.9)$$

$$a^{\dagger(\lambda)}(\mathbf{p}) |m(\mathbf{p}, \lambda)\rangle = \sqrt{m+1} |(m+1)(\mathbf{p}, \lambda)\rangle. \quad (3.10)$$

Now that we have adequately described the Hamiltonian and the quantized field, we can proceed to calculate the quantum probability amplitude \mathcal{M} which will ultimately give us the E1-E1 coupling tensor and therefore the transfer rate for resonant energy transfer. The probability amplitude \mathcal{M} appears, for example, in Fermi's Golden Rule (see for example equation 2.1 on page 5).

In order to calculate \mathcal{M} , we need to describe what is happening with initial and final states from which \mathcal{M} will be obtained. In keeping with the notation established in equation 3.7, consider our system² where the donor is labeled D and the acceptor is labeled A . The ground (relaxed, unexcited) state of the donor and the acceptor is denoted by 0 , and the excited states of the donor D and acceptor A are denoted by α and β respectively. In this fashion, the initial state $|i\rangle$ can be written as $|D^\alpha; A^0; 0\rangle$, and the final state $|f\rangle$ can be also written as $|D^0; A^\beta; 0\rangle$.

²The energy transfer process here is assumed to operate between two and only two atoms/molecules/NCs, i.e. there is one Donor and one Acceptor.

Clearly, the process of energy transfer will necessarily require the action of (at least) one annihilation operator and one creation operator.

What was explained in the previous paragraph can be more easily understood by looking at figure 3.1. The Feynman diagrams represent the two time orderings which must be considered here for the E1-E1 energy transfer process. Figure 3.1(a) shows explicitly how the system starts with D in an excited state α , and a virtual photon (of momentum \mathbf{p} and polarization λ) is created at D and is annihilated at A , promoting the acceptor state A to its excited state β . Figure 3.1(b) represents the other time ordering which must be included in the analysis, where a virtual photon propagates from A to D . Field theory processes in general must include all time ordered components in order to correctly represent the underlying process(s). Although the process in figure 3.1(b) appears to be counter-intuitive at first glance, it must be considered in the calculations that follow where, by virtue of the time-energy uncertainty principle (see below) a virtual photon is involved in the transfer of energy.³

The term "virtual" photon must be understood as energy that is borrowed from the vacuum as predicted by quantum theory. Indeed, the uncertainty principle is most known in the form $\Delta x \Delta p \geq \hbar$. This last equation can be rewritten as

$$\frac{m \Delta x}{p} \frac{p \Delta p}{m} \geq \hbar. \quad (3.11)$$

Since $E = p^2/2m$, then $\Delta E = p \Delta p/m$. Therefore,

$$\Delta t \Delta E \geq \hbar. \quad (3.12)$$

³Any Feynman diagram for any process must include all time orderings for a correct representation of the process. See for example the excellent book by Peskin and Schroeder [60].

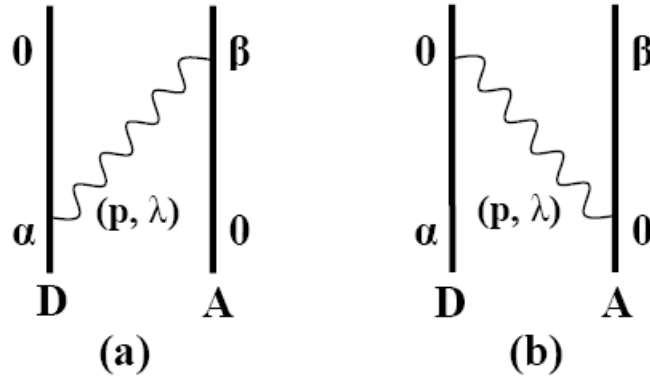


Figure 3.1. Feynman diagrams showing the two time orderings involved in resonant energy transfer (dipole-dipole), where 0 is the ground state level, α and β are the excited state levels for the Acceptor and Donor respectively. The virtual photon has momentum \mathbf{p} and polarization λ . Time flows from left to right. **(a)** Case where the Donor is first excited and energy is subsequently transferred to the Acceptor. **(b)** Case where the Acceptor is first excited (see text).

This last equation is the time-energy uncertainty principle. Applied to our theory, a virtual photon of a given energy can be created from vacuum as long as the time during which it exists respects the above equation. In other words, in the present case of resonant energy transfer, the virtual photon will exist for a time (its "time of flight") determined by the distance between D and A .

Quantum theory, for time dependent perturbations, tells us that the probability amplitude for any process can be written as

$$\mathcal{M} = \langle f | H_{interaction} | i \rangle + \sum_s \frac{\langle f | H_{interaction} | s \rangle \langle s | H_{interaction} | i \rangle}{E_i - E_s} + \dots, \quad (3.13)$$

where the summation is over intermediate states $|s\rangle$ and the energies E are those of the state identified by the subscript. These intermediate states represent the sequences of the transitions (there are obviously two here) that the donor and acceptor experience.

In the present case, since the probability amplitude \mathcal{M} involves virtual photons and that their interaction is represented via the second term in equation 3.13,⁴ then \mathcal{M} can be written the following way, taking into consideration both time orderings as shown in figure 3.1

$$\mathcal{M} = \frac{\langle f | H_{interaction} | a \rangle \langle a | H_{interaction} | i \rangle}{E_i - E_a} + \frac{\langle f | H_{interaction} | b \rangle \langle b | H_{interaction} | i \rangle}{E_i - E_b}. \quad (3.14)$$

From the notation used, the first and second terms in equation 3.14 correspond to the processes shown in figures 3.1(a) and (b) respectively. Referring to figure 3.1, the energies E can be written as $E_i = E_\alpha^D + E_0^A$, $E_a = E_0^D + E_0^A + \hbar cp$, and $E_b = E_\alpha^D + E_\beta^A + \hbar cp$. $\hbar cp$ is the energy of the virtual photon. It is possible to rewrite these last equations, using energy conservation, as $E_\alpha^D - E_0^D = E_\beta^A - E_0^A = \hbar ck$, where $\hbar ck$ is the physical, measurable transferred energy.

By combining the definitions of $|i\rangle$ and $|f\rangle$ of page 31 along with the definitions of the various energies as defined in the previous paragraph, substituting them into equation 3.14, and using the quantum electric field operator of equation 3.8 and applying the relevant actions of the creation and annihilation operators we get

$$\mathcal{M} = \frac{1}{2\varepsilon_0 V} \sum_{\mathbf{p}, \lambda} p \mathcal{E}_i^{*(\lambda)}(\mathbf{p}) \mathcal{E}_j^{(\lambda)}(\mathbf{p}) \times \left\{ \frac{\mu_i^{0\alpha} \mu_j^{\beta 0} e^{i(\mathbf{p} \cdot \mathbf{R})}}{k - p} + \frac{\mu_j^{0\alpha} \mu_i^{\beta 0} e^{-i(\mathbf{p} \cdot \mathbf{R})}}{-k - p} \right\}. \quad (3.15)$$

In this last equation, the Einstein convention of summation over repeated indices is obvious, and a shorthand notation is used for the electric dipole transition moments where, for example, $\mu^{0\alpha} = \langle A^0 | \boldsymbol{\mu}^{(D)} | D^\alpha \rangle$. The position vector $\mathbf{R} = \mathbf{R}_A - \mathbf{R}_D$ is simply the vector representing the distance between acceptor and donor.

⁴The first order term in equation 3.13 represents a direct interaction between the donor and acceptor via a direct photon.

We will now modify equation 3.15 by doing a few substitutions. First, by doing $V \rightarrow \infty$, the summation can be converted into an integral by invoking a well known identity⁵

$$\lim_{V \rightarrow \infty} \frac{1}{V} \sum_{\mathbf{p}} = \int \frac{d\mathbf{p}}{8\pi^3}. \quad (3.16)$$

Secondly, since that there are terms in equation 3.15 that involve the product of two unit polarization vectors, we can rewrite these products (and the summation over their products) the following way [62]. For clarity, let us consider the following wave vector \mathbf{p} in spherical coordinates

$$\mathbf{p} = p (\sin \theta, \sin \theta \sin \phi, \cos \theta). \quad (3.17)$$

A possible set of unit polarization vectors are (recall that the polarization vectors must be orthogonal to each other and to \mathbf{p} , i.e. $\mathcal{E}^{(\lambda_1)}(\mathbf{p}) \cdot \mathcal{E}^{(\lambda_2)}(\mathbf{p}) = \delta_{\lambda_1, \lambda_2}$ and $\mathcal{E}^{(\lambda)} \cdot \mathbf{p} = 0$)

$$\mathcal{E}^{*(\lambda_1)}(\mathbf{p}) = (\sin \phi, -\cos \phi, 0) \quad (3.18)$$

and

$$\mathcal{E}^{*(\lambda_2)}(\mathbf{p}) = (\cos \theta \cos \phi, \cos \theta \sin \phi, -\sin \theta). \quad (3.19)$$

It is easy to show that the following holds

$$\mathcal{E}_i^{(\lambda_1)}(\mathbf{p}) \mathcal{E}_j^{*(\lambda_1)}(\mathbf{p}) \cdot \mathcal{E}_i^{(\lambda_2)}(\mathbf{p}) \mathcal{E}_j^{*(\lambda_2)}(\mathbf{p}) = \delta_{ij} - \mathbf{p}^2. \quad (3.20)$$

Note that this last equation will hold for any choice of proper polarization vectors.

We can now address the sum over the polarizations

$$\sum_{\lambda} \mathcal{E}_i^{(\lambda)}(\mathbf{p}) \mathcal{E}_j^{*(\lambda)}(\mathbf{p}) = \delta_{ij} - \hat{p}_i \hat{p}_j, \quad (3.21)$$

⁵See for example [61], Chapter 2.

where \mathbf{p}^2 was written as $\hat{p}_i \hat{p}_j$ by assuming that \mathbf{p} (for example equation 3.17) is a unit vector. We can combine equation 3.16 and the above equation into equation 3.15 to get

$$\mathcal{M} = \frac{\mu_i^{0\alpha} \mu_j^{\beta 0}}{2\varepsilon_0} \int p (\delta_{ij} - \hat{p}_i \hat{p}_j) \left\{ \frac{e^{i(\mathbf{p} \cdot \mathbf{r})}}{k - p} + \frac{e^{-i(\mathbf{p} \cdot \mathbf{r})}}{-k - p} \right\} \frac{d^3 \mathbf{p}}{8\pi^3}. \quad (3.22)$$

The above integral can be performed, but two more tricks must be used. First, the integral is converted to spherical coordinates (i.e. $d^3 \mathbf{p} \rightarrow p^2 d\mathbf{p} d\Omega$). Second, by use of the gradient operator, we can write

$$\int \hat{p}_i \hat{p}_j e^{\pm i(\mathbf{p} \cdot \mathbf{R})} d\Omega = -\frac{1}{p^2} \nabla_i \nabla_j \int e^{\pm i(\mathbf{p} \cdot \mathbf{R})} d\Omega. \quad (3.23)$$

The integral can now be evaluated. Changing variables and performing the integrals over the angles gives

$$\mathcal{M} = \frac{\mu_i^{0\alpha} \mu_j^{\beta 0}}{4\pi^2 \varepsilon_0} (-\nabla^2 \delta_{ij} + \nabla_i \nabla_j) \int_{-\infty}^{\infty} \frac{\sin pR}{2R} \left\{ \frac{1}{k - p} + \frac{1}{-k - p} \right\} dp. \quad (3.24)$$

The integral in the last equation is in fact a Green function which must be evaluated by a proper choice of the contour in the complex plane. In fact, care must be taken in order to make the correct choice of the contour.⁶ The result is given by

$$-\frac{\pi}{R} e^{\pm ikR}. \quad (3.25)$$

Applying the Laplacian and the gradient operators of equation 3.24 onto the above result yields

$$\begin{aligned} \mathcal{M} &= \frac{e^{ikR}}{4\pi \varepsilon_0 R^3} \left\{ (\delta_{ij} - 3\hat{R}_i \hat{R}_j) - ikR(\delta_{ij} - 3\hat{R}_i \hat{R}_j) - (kR)^2(\delta_{ij} - \hat{R}_i \hat{R}_j) \right\} \\ &\quad \times \mu_i^{0\alpha} \mu_j^{\beta 0} \\ &= \mu_i^{0\alpha} V_{ij}(k, \mathbf{R}) \mu_j^{\beta 0}, \end{aligned} \quad (3.26)$$

⁶See Appendix A on page 76 for a discussion on how the integral is evaluated.

where $V_{ij}(k, \mathbf{R})$ is defined as the coupling tensor and is in fact the final result from which the interesting FRET effect is deduced.

Going over many interesting physical discussions arising from the coupling tensor $V_{ij}(k, \mathbf{R})$ [55], the E1-E1 transfer rate coupling is now derived. We start with Fermi's golden rule

$$\Gamma = \frac{2\pi}{\hbar} |\mathcal{M}|^2 \rho_{FinalStates}, \quad (3.27)$$

which must be rewritten to account for the fact that in our interacting electric dipole system, a rotational averaging must be performed [63], yielding

$$\Gamma = \frac{2\pi |\boldsymbol{\mu}^{0\alpha}|^2 |\boldsymbol{\mu}^{\beta 0}|^2 \rho_{FinalStates}}{9\hbar} A(k, R), \quad (3.28)$$

where $A(k, R)$ is our quantity of interest, the excitation transfer function [57]

$$\begin{aligned} A(k, R) &= V_{ij}(k, \mathbf{R}) V_{ij}^*(k, \mathbf{r}) \\ &= \frac{2}{(4\pi\epsilon_0 R^3)^2} \left\{ 3 + (kR)^2 + (kR)^4 \right\}. \end{aligned} \quad (3.29)$$

This last equation is the final result of the calculations of the past five pages. There are three terms in equation 3.29. The first term dominates in the short range limit, i.e. when $kR \ll 1$. This first term leads to the R^{-6} dependence of the energy transfer rate first proposed by Förster [48]. It is this first term that represents the transfer of energy of a virtual photon since the limit in which this term is valid ($kR \ll 1$) corresponds to the close proximity of the donor D and acceptor A where energy transfer follows the time energy uncertainty principle stated in equation 3.12. From a physical point of view, the other two terms in equation 3.29 are also interesting. The last term corresponds to the long range limit (i.e. when $kR \gg 1$), which corresponds to the classical case of the R^{-2} dependence of transfer of radiation (via a "real" photon).

The second term in equation 3.29 is the "intermediate" term. If the excitation transfer function $A(k, R)$ were to be plotted, the two distinct near and far regions (i.e. for $kR \ll 1$ and $kR \gg 1$) would be obvious for small and large separation distances between respectively. The transition of the curve between the near and far regions is where the second term of equation 3.29 shows more importance.

Applied to the our specific case of FRET, we can write the expression for the energy transfer rate in the near zone ($kR \ll 1$)

$$\Gamma_{NearZone} = \frac{|\boldsymbol{\mu}^{0\alpha}|^2 |\boldsymbol{\mu}^{\beta 0}|^2}{12\pi\hbar\epsilon_0^2 R^6} \rho^{FinalStates}. \quad (3.30)$$

The excitation transfer function $A(k, R)$ in equation 3.29 is in actuality a relativistically correct result for the type of dipolar coupling that was considered here (E1-E1) and that the Förster result is in fact a near zone approximation [51]. Equation 3.29 is the correct result for the transfer of energy between molecules in vacuum. It is possible however, by explicit inclusion of the vibrational structure for the molecular state vectors of the donor and acceptor, to obtain the same result for the energy transfer rate as that of equation 3.1 [64,65]. What becomes clearer is that when obtaining the Förster result (equation 3.1) from QED calculations, as expected, the electric dipole transition moments of equation 3.30 simply become part of the term $\epsilon_A(\lambda)$ in the Förster result.

We have shown a summary of calculations based on first principles that have led to a clearer description of FRET. We now move onto experimental result which show an application of such FRET.

3.3 Experiment and Results

The experiment that was conducted has allowed FRET between NCs of two different sizes placed in a 1D Fabry-Pérot microcavity. The latter is in fact quite similar to the one described in the previous chapter. ZnS capped CdSe NCs of 3.6 nm and 4.6 nm were used, with emission and absorption spectra as shown in figure 3.2.

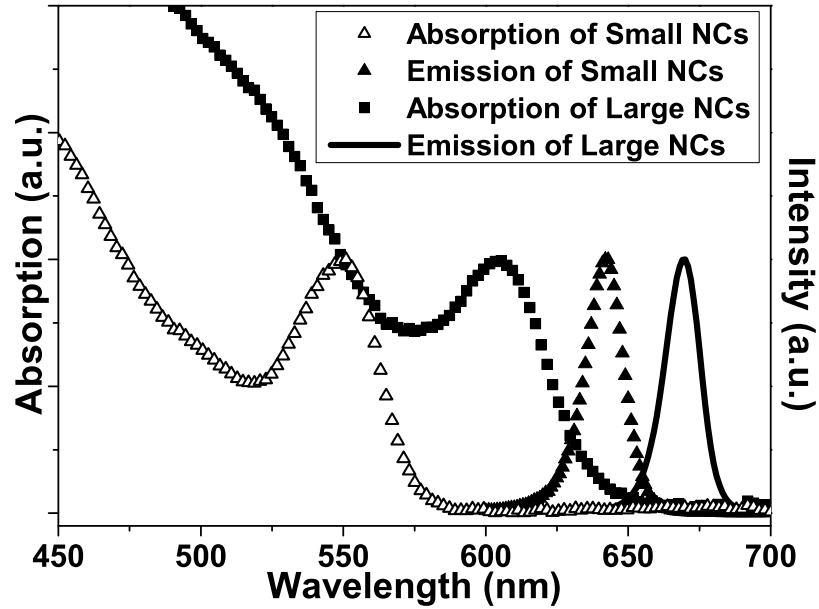


Figure 3.2. Photoluminescence and absorption spectra of the two different sized NCs that were used in the FRET experiment (from [66]).

In anticipation of the effect of the microcavity on the emissions of the NCs and as preparatory work on FRET, measurements using an argon laser at 514.5 nm were performed on samples which did not involve a microcavity. The solid line in figure 3.3 shows the photoluminescence spectrum of the mixed NCs in a colloidal suspension, where the emission from the smaller dots is much stronger than the emission of the larger dots. In sharp contrast to this, the line of triangle symbols in

the same figure shows the photoluminescence spectrum of the mixed NCs formed into a monolayer using the Langmuir-Blodgett technique. Clear evidence of energy transfer is apparent from the obvious change in the heights of the emission of the small and large dots from the film.

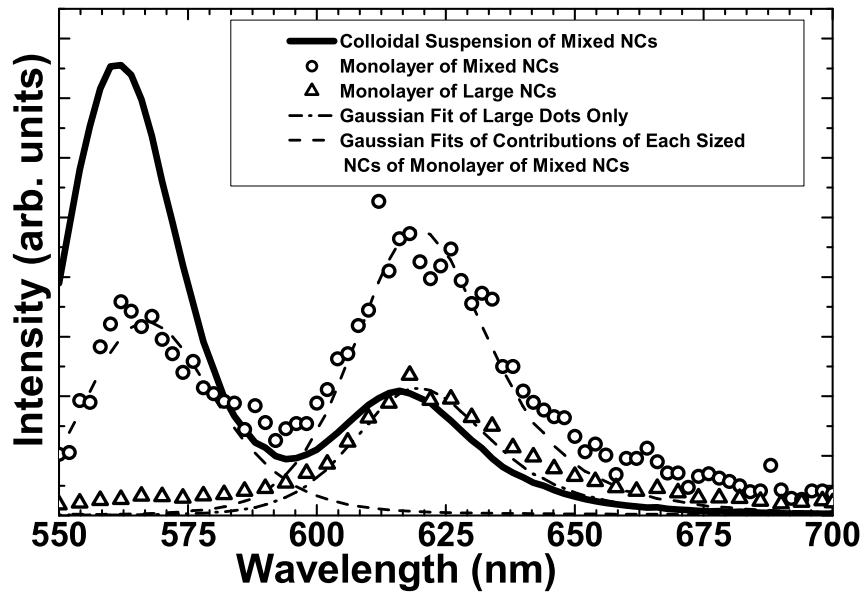


Figure 3.3. Free space photoluminescence spectra of: a colloidal suspension of mixed NCs (solid line), a monolayer of mixed NCs (open circles), and a monolayer of the larger (4.6 nm) NCs only (triangles) (from [66]).

In view of the effect of mixing NCs of two different sizes (figure 3.3), NCs were incorporated in a microcavity to further enhance the luminescence of the large NCs. The microcavity was formed between two DBR's of alternating layers of SiO_2 and TiO_2 deposited as described on page 14, with a target thickness of the quarter wavelength layers using $\lambda=620$ nm. After the first half of the SiO_2 cavity was deposited, a monolayer of NCs using standard Langmuir-Blodgett techniques

followed. Two types of samples were prepared in this fashion, one consisting on NCs of 4.6 nm only, and the other consisting of a mix of the 3.6 nm and 4.6 nm NCs with a molar ratio of 4:3. After drying of the solvents, the rest of the SiO₂ microcavity was deposited and the rest of the layers to form the second DBR. Reference samples were also prepared (with only the 4.6 nm NCs and with the mixed NCs) by covering a glass substrate using the same Langmuir-Blodgett technique and capping the samples with 75 nm of SiO₂.

Figure 3.4 shows the photoluminescence measurements that were performed on the microcavity, where direct evidence of FRET is clear. The circles in figure 3.4 is the photoluminescence of a monolayer of the large dots in free space. The solid line in the figure shows the effect of the microcavity on the emission of the monolayer of large dots, while the dashed line shows the emission of the mixed dots inside the microcavity, with the cavity's resonance tuned to the emission peak of the large dots. Note that the quality of the NC coating process using the Langmuir-Blodgett technique is such that the microcavity suppresses emission at wavelengths that are not in tune with its resonance.

It is possible to calculate the expected energy transfer efficiency between the small and large NCs using the following equation [49]

$$E = \frac{R_0^6}{R_0^6 + R_{DA}^6}, \quad (3.31)$$

where R_{DA} is the distance separating the donor and acceptor, and R_0 is the critical donor-acceptor distance, which is defined as the distance when the rate of energy transfer is equal to the sum of all radiative and nonradiative energy transfers rates. To this end, R_0 can be obtained with the following formula [49]

$$R_0 = 9.78 \times 10^3 \left[\frac{\kappa^2}{n^4} Q_D J(\lambda) \right]^{\frac{1}{6}}, \quad (3.32)$$

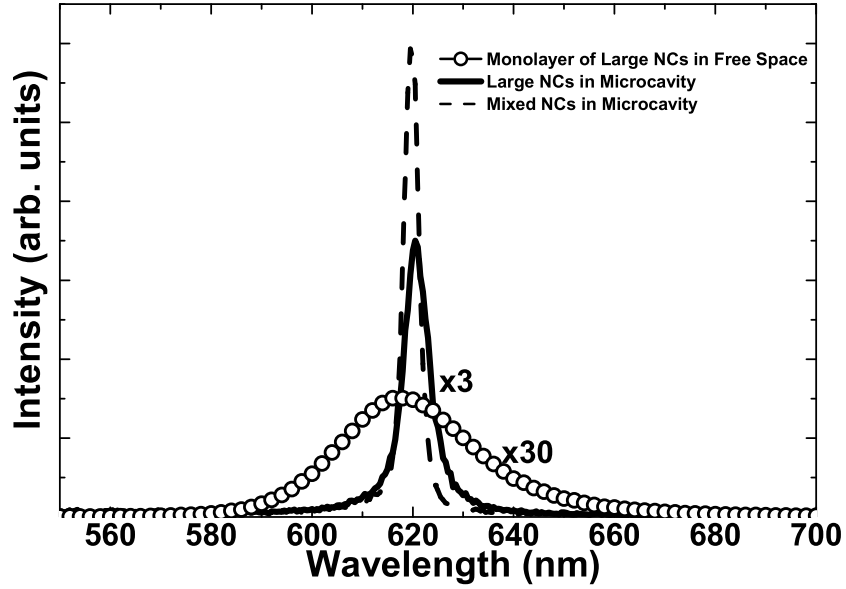


Figure 3.4. Normalized fluorescence spectra from monolayers of NCs. The open circles represent the photoluminescence of large dots in free space. The solid line is the photoluminescence from the large NCs only inside a microcavity. The dashed line represents the photoluminescence from the mixed NCs inside a microcavity (from [66]).

where κ^2 is the relative orientation of the donor and acceptor and equals $2/3$ in the present case, n is the index of refraction of the NC monolayer and equals 2.8 [24], Q_D is the luminescence quantum yield of the donor, and $J(\lambda)$ is the spectral overlap between the emission spectra of the donor and acceptor. Q_D , after ZnS capping, was evaluated to be of 27% (relative to rhodamine 590) [66], and $J(\lambda)$ is easily obtained from figure 3.2. With these values, this gives a value for R_0 of 5.8 nm, which agrees well with the value of 4.7 nm in previous work on CdSe quantum dot solids [44].

The last value that is needed to calculate the energy transfer efficiency E in equation 3.31 is R_{DA} . Taking into consideration the diameters of the CdSe NC cores (3.6 and 4.6 nm), the thickness of the ZnS capping layer (0.45 nm [67]) and including an additional separation between the NCs of 1.1 nm due to the organic surface capping molecule (trioctylphosphine oxide - TOPO) [44], this results in a value of 6.1 nm for R_{DA} . Using the above values in equation 3.31 gives a result of 23% for the energy transfer efficiency.

Returning to figure 3.3, where a clear increase in the photoluminescence of the large NCs in the mixed NC monolayer is obvious, it is possible to calculate the integrated emission enhancement of the large NCs. Note that the photoluminescence spectrum of the monolayer of purely large NCs is normalized so that it represents emission from the same number of large NCs as the spectrum from the mixed NCs monolayer (molar ratio of small to large NCs of 4:3). Gaussian fits of the spectra, centered at the emission peak of the small and large NCs, allows for the calculation of the contribution of both sizes of NCs to the mixed NC emission spectrum in order to determine the relative increase in the emission (per large NC) of the large NCs in the mixed NC monolayer. The relative integrated emission of the mixed NC monolayer is increased by a factor of 2 ± 0.3 over that of the purely large NC monolayer.

The photoluminescence enhancement can be calculated from figure 3.4. The integrated emission from the sample with only large NCs inside the microcavity is enhanced by a factor of 4.8 ± 0.6 with respect to the reference sample (also consisting of purely large NCs). The FWHM of the emission is also considerably narrowed from 33 nm to 5.5 nm. From the same figure, the photoluminescence enhancement can also be obtained by once again comparing the emission in free

space (reference sample) and in the microcavity of the mixed NC monolayer. The integrated emission for the mixed NCs inside the microcavity is enhanced by a factor of 2.7 ± 0.4 when compared to the emission of the purely large NCs inside the microcavity. This enhancement factor is the result of FRET. In all, the increase in the integrated photoluminescence as a result of placing the large NCs in the cavity (4.8) combined with the increase of the integrated photoluminescence resulting from FRET (2.7) results in a total enhancement of a factor of $4.8 \times 2.7 = 13$. In other words, this last value reflects the total integrated emission enhancement which results from placing the large NCs (acceptors) in close proximity to the small NCs (donors) inside a microcavity.

We can compare the experimental enhancement results to theoretical calculations. The value for the enhancement due to FRET was already calculated on the previous page. The theoretical value of the enhancement due to the cavity need to be calculated. As was shown in the previous chapter, the integrated emission enhancement in a 1D microcavity Γ/Γ_0 can be calculated using equation 2.13 on page 21. The finesse $F = \lambda_0 Q / 2nd = 13.7$ using $Q = \lambda_0 / \Delta\lambda_{PL}$. The field enhancement factor is estimated to be $\xi = 1$ since the NCs monolayer was placed at the center of the microcavity. This results in a value for the effect of the microcavity on the photoluminescence of an enhancement of $\Gamma/\Gamma_0 = 10.9$. This value combined with the calculated value of 2 for the effect of the energy transfer enhancement (neglecting the effect of the cavity on the energy transfer rate) gives a final expected theoretical enhancement value of 22. This value agrees reasonably well with the experimental enhancement value of 10.9. The slight theoretical overestimation of the enhancement is attributed in the assumption that $\xi = 1$, meaning that the NC layer may not be exactly at the center of the microcavity but rather experiences a

spreading around the center of the microcavity. There could be also an additional contribution to this small discrepancy which arises from the fact that, for emitters which have high (~ 1) quantum yield, as is almost the case for the NCs studied here, the enhancement that is due to the microcavity is predicted to be relatively independent of the local optical mode density [68].

These experiences on FRET are exciting in that they allow for the excitation of a given species of emitter via a donor, with the latter's emission spectrum coinciding with the absorption spectrum of the former. The sensitivity of the efficiency of the transfer rate of energy between the donor and the acceptor is such (see for example equation 3.31 on page 41) that precise control of the distance separating both species must be exercised. The Langmuir-Blodgett technique for the obtention of monolayers in conjunction with microcavities allow for such control. It would be possible to further increase the output of the device by optimizing the ratio of the small (donor) to large (acceptor) NCs in order to maximize the transfer of energy. The sizes as well as the number of the different species of NCs can also be tuned and/or optimized in order to obtain good spectral overlap between the donor(s) and acceptor(s). It would be possible also to use multiple layers of mixed NCs of different/several sizes.

RARE EARTH DOPED GAN IN THE FORM OF A POWDER

4.1 Introduction

Group III nitrides have wide applications in optoelectronic devices, such as light-emitting diodes, ultraviolet or blue lasers, and full color displays [69–71]. The recent demonstration of visible (blue, green, red) and infrared (1.54 μm) electroluminescence from rare earth (RE)-doped GaN brings significant interest to this class of materials for possible applications in optical communications and full color displays [71–73]. RE ions have higher luminescence efficiency as compared to other semiconductors such as Si or GaAs [74]. Er, Eu, Tm and other RE elements have been doped into GaN by several research groups [73].

The GaN-based semiconductor structures are of great interest because they appear to be optically robust, and chemically and thermally stable. The band gaps of III nitrides range from the ultraviolet to the near infrared. Wide band gap semiconductors, like gallium nitride (GaN), doped with rare earth RE elements are especially interesting because of the decreased quenching effects of the luminescence at room temperature [75]. The wide band gap of GaN leads to a reduced RE quenching of emission and thus to the observation of strong RE emission at room temperature [75].

The doping of GaN with RE elements allows the possibility for light emission in the red (Eu) [76], green (Er) [77] and blue Tm) [78] portions of the visible spectrum. Electroluminescent devices using these materials have been shown (see the references in the previous sentence), and color integration for the eventual purpose of large flat panel displays.

In the works cited in the previous paragraphs, the incorporation of Er atoms into GaN is achieved either *in situ* by epitaxial growth with the GaN layer or ion implantation after the layer growth step. In most of cases, GaN is in the form of an epilayer on top of different substrates sapphire, Si, or SiC. Among the methods reported for the fabrication of the material are metalorganic chemical vapor deposition MOCVD [79,80], molecular beam epitaxy MBE [73,78,81–85], sputtering [86] and hybrid vapor phase epitaxy [87]. The RE elements can be incorporated into the GaN film either *in situ* or they can be implanted after the growth of the film.

To date, RE doping in GaN powder has been rarely investigated. The incorporation of RE materials in GaN powder could enable hybrid integration with a variety of optically inactive materials. There are, however, few reports that focus on RE doped GaN in the form of a powder. GaN:RE powder enables the possibility of hybrid integration with a variety of optically inactive materials because of the flexible powder form. Hirata et al. used a combustion system to make GaN:Eu and Ga₂O₃:Eu powder [88]. GaN powder doped with Eu also has been prepared by El-Himri et al. using ammonolysis of the freeze-dried precursors [89].

Here experimental results are presented on RE (Er and Eu) doped GaN in the form of a powder [90–94]. In both cases, the main fabrication steps of the GaN:RE powders involve heating at 830 C for several hours and cooling a mixture of gallium (99.9999%), bismuth shot (99.999%) and RE (99.9%) ingot in an ammonia ambient to initially obtain chunks of the desired material. The cooled chunks are then manually ground into a fine powder using a mortar and pestle, and the bismuth is removed by evaporating it from the material by heating it for several hours at 1030 C under flowing NH₃. More details on the fabrication of the materials can be found in [90,91,93–95]. A great advantage of the powder form of this type of material is

that it can, for example, be combined with cellulose to obtain a mélange which is easily spun into a thin film onto any substrate. After the spin coating process, the cellulose can be easily baked off with a moderate temperature anneal [96].

4.2 Er doped GaN Powder - Experiment and Results

In both cases for the Er and Eu doped GaN powders, x-ray diffraction (XRD) analyses were performed and showed that no elemental Er or Eu, Ga, Bi or EuN or ErN were detected, and all of the peaks in the XRD patterns matched the GaN peaks as reported in the American Society for Testing and Materials. As shown in figure 4.1, the diffraction pattern shows clear evidence of the wurtzite structure for the Er doped GaN (1at.%). The (0002) peak is much stronger than the $10\bar{1}1$ peak although the latter should be the strongest peak.

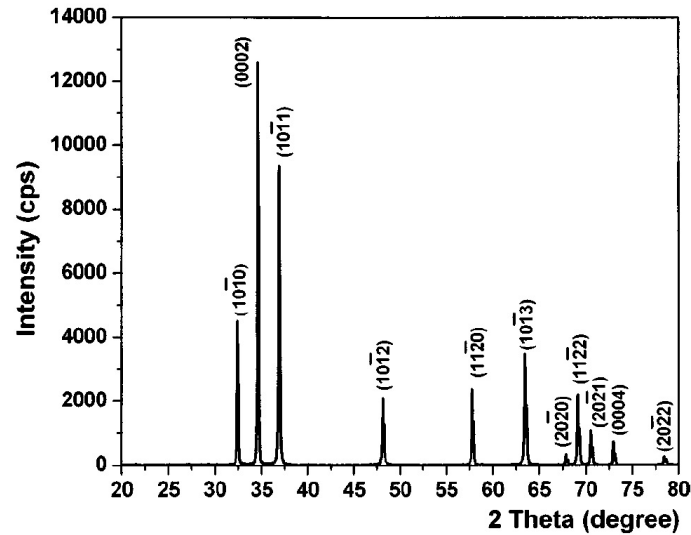


Figure 4.1. Representative X-ray diffraction pattern for the case of the GaN:Er powder after the removal of Bi. All of the peaks match with the wurtzite GaN structure, and no traces of Ga, Bi or Er is detected (from [91]).

From the last figure, this shows that there is a preferred orientation in the powder sample, as is explained with the scanning electron microscope (SEM) images below. Figure 4.2 shows that the particles have a size distribution that varies between approximately 1 and 10 μm with an average around 5 μm . Several morphologies are observed, namely plates, polyhedra, needles and, mostly, platelets. The aspect ratio of the plates is estimated to vary between 5 and 10. From this, the dominant (0002) orientation in the XRD pattern is assigned to the alignment of the plates during sample preparation.

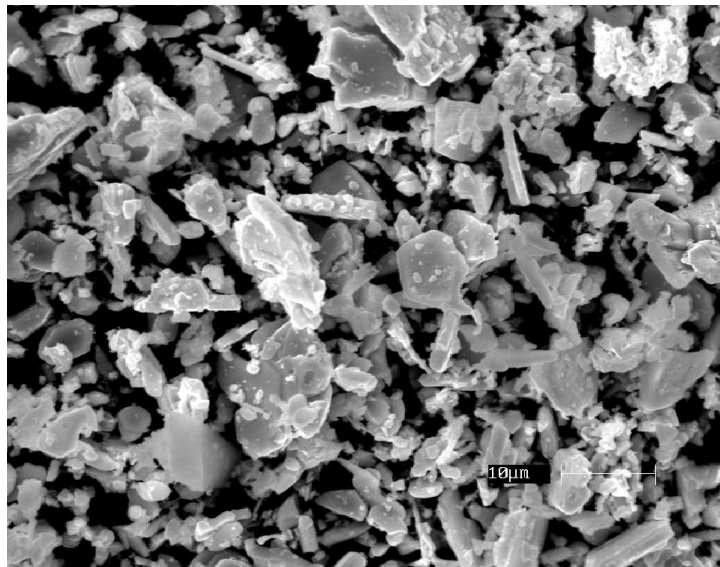


Figure 4.2. Scanning electron microscopy image of the morphology of the synthesized GaN:Er powder; particle sizes range from 1 to 5 μm and platelet particles are the majority (from [91]).

Photoluminescence measurements were performed on the GaN:Er powder using an argon laser tuned at 496.5 nm (2.5 eV), an excitation energy below the bandgap of GaN at 3.4 eV. Room temperature visible photoluminescence from the sample is shown in figure 4.3. Two major emission lines are obvious at 537 and 558 nm,

with the former corresponding to a transition between the ${}^2H_{11/2}$ and the ground level ${}^4I_{15/2}$, and the latter corresponding to a transition between ${}^4S_{3/2}$ and ${}^4I_{15/2}$ of the $4f$ inner shell of the Er^{3+} ions.¹ The FWHM of the peaks are 2.6 and 3.1 nm respectively, which correspond to energy widths of 11 and 13 meV. The emission peaks in this spectrum are similar to already reported data from MOCVD [80] or MBE GaN:Er films [77, 97].

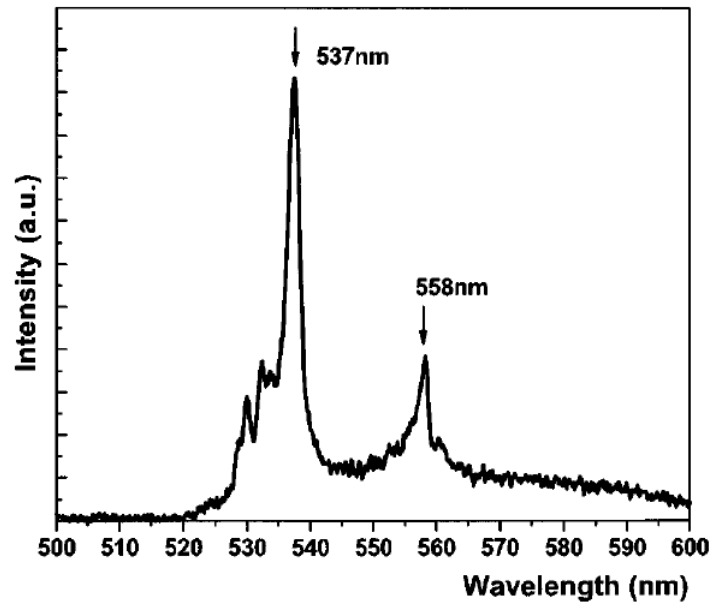


Figure 4.3. Room temperature photoluminescence spectrum of the Er doped GaN powder. The emissions at 537 and 558 nm are characteristic of $4f$ inner shell transitions in the Er^{3+} ions (from [91]).

¹An excellent diagram showing the various energy levels of the Erbium $4f$ inner shell transitions is shown in [77].

4.3 Eu doped GaN Powder - Experiment and Results

In a similar way to how the Er doped GaN powder was fabricated, Eu was used as a dopant. In contrast to the Er doped GaN powder (see figure 4.3), the emission from the Eu^{3+} ions in the GaN show marked, sharp, strong emission peaks as shown below.

The SEM images shown in figure 4.4, especially the zoom on the right, reveal the many layers in the particles which are a result of the fact that the particles grows in successive layers.

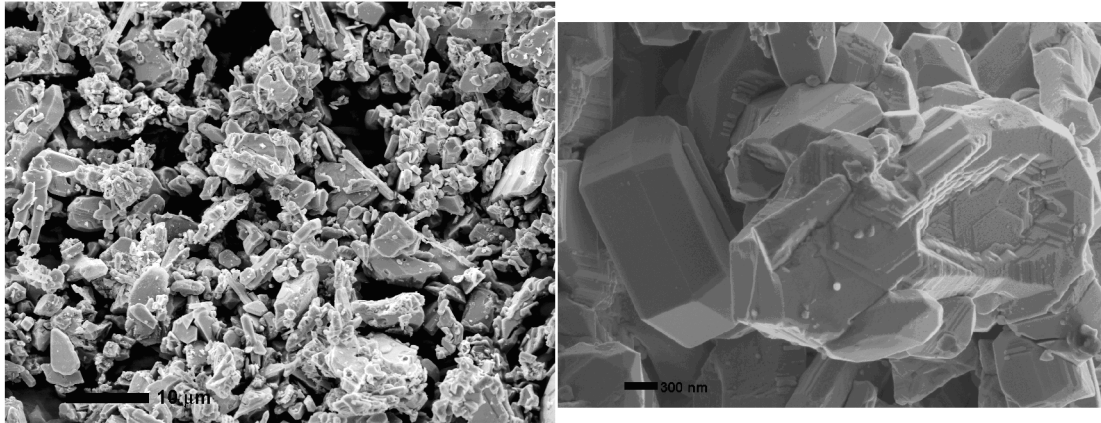


Figure 4.4. SEM images of the Eu doped GaN powder (2 at.%). The top picture shows the overall morphology of the powder, while the lower picture is a zoom showing the highly faceted and hexagonal structure of the particles (from [90]).

Photoluminescence characterizations were performed both below and above the host material's bandgap at room temperature. An argon laser at 457.9 nm was used for the below bandgap measurements, and a HeCd laser at 325 nm was used for the above bandgap measurements. The size of the excitation spot was 1 mm in both cases. The photoluminescence setups involve the excitation of the sample, the collection and collimation of the emission with a lens and the filtering

of the excitation wavelength from the collimated, non focused beam. The filtering was effected using a Corning 3-70 sharp cut yellow filter to block out the below bandgap excitation, while a 0-52 UV blocking filter was used to filter out the above bandgap excitation. Measurements were performed using a 0.64 m ISA Instruments spectrometer (in monochromator mode) with input and output slits were set at $500 \mu\text{m}$. The output of the monochromator was sent to a Hamamatsu R920 photomultiplier tube.

Figure 4.5 shows the resulting spectra from the above and below bandgap excitations. In passing, the efficient removal of the excitation wavelengths from the spectra is obvious (in the case of the HeCd excitation, there would have been a second order diffraction appearing from the HeCd excitation at $2 \times 325 = 650 \text{ nm}$). Strong red light is visible to the naked eye from the sample whether it is excited above or below bandgap. The red color is mostly due to the 621 nm peak which is the strongest of the Eu emissions. The FWHM of this peak are 2.2 and 8.1 nm for the above and below bandgap excitations respectively. It is interesting to note that the peak intensity for the emission from the above bandgap excited sample is much stronger than its counterpart. This indicates an efficient electro-optical transfer process in which the excitation energy is absorbed by the host material (GaN) and is quickly transferred to the Eu^{3+} ions [98]. More on this matter in the next section.

The main emission line of the Eu^{3+} ions at 621 nm corresponds to the ${}^5D_0 \rightarrow {}^7F_2$ transition within the $4f$ shell of the ions. The bandedge emission from the GaN is weak and broad compared to the emission lines of the Eu^{3+} . There are also obvious emission peaks on figure 4.5 at 542, 601 and 663 nm, which are respectively attributed to the ${}^5D_1 \rightarrow {}^7F_1$, ${}^5D_0 \rightarrow {}^7F_1$ and ${}^5D_0 \rightarrow {}^7F_3$ transitions in the $4f$ level

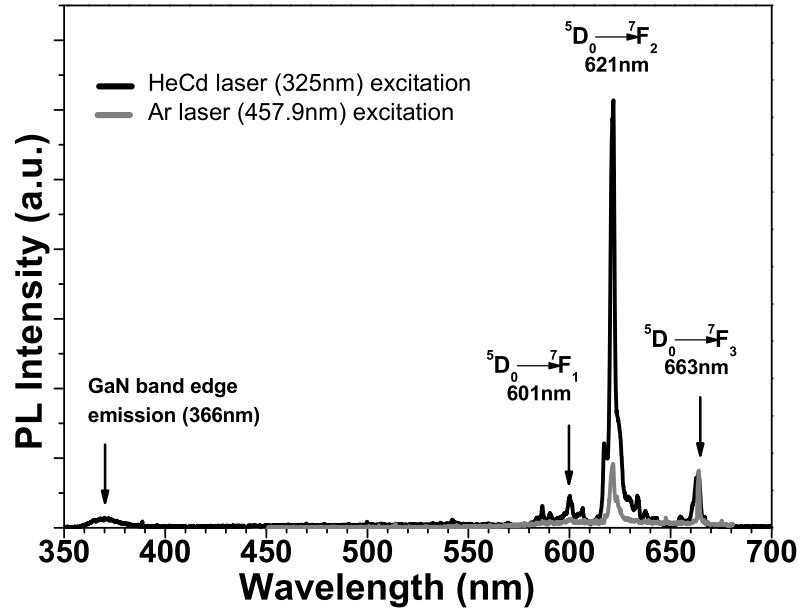


Figure 4.5. Room temperature photoluminescence spectra of the GaN powder doped with Eu (1 at.%). The dark line corresponds to the emission from the above bandgap excitation (325 nm), while the gray line is the emission from the below bandgap excitation (457.9 nm) (from [90]).

of the Eu³⁺ ions. The spectra in figure 4.5 agree well with the majority of the referenced literature [73, 76, 79].

In order to see the effect of the doping concentration of the Eu³⁺ ions in the GaN powder, samples were prepared with different concentrations of the ions, varying from 0 to 3 at. % of Eu³⁺. Figure 4.6 shows the photoluminescence spectra of the various samples under HeCd excitation (above bandgap). For comparison, a pure sample of GaN without any doping was also measured. For this last sample, the bandedge emission is strong (scaled to 1/3 of its peak in order to fit it on the same graph). This bandedge emission decreases dramatically as the concentration of the

Eu^{3+} ions is increased. This in fact is a direct consequence of energy transfer (not the type of transfer described in chapter 2 of this dissertation) between the host material and the Eu^{3+} ions (see the next section).

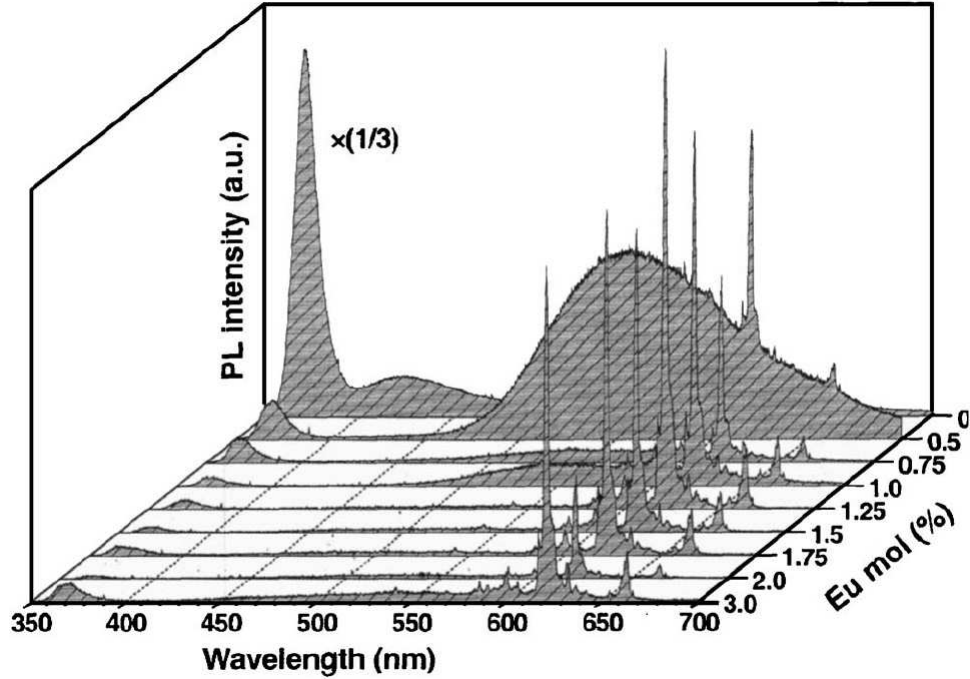


Figure 4.6. Room temperature photoluminescence spectra of the GaN powder doped with different concentrations of Eu^{3+} (from [90]).

The emission peaks in figure 4.6 intensify with increasing concentration of Eu^{3+} ions, up to 1.25 %, and then weaken for higher doping concentrations. This is due to cross relaxation between neighboring Eu^{3+} ions which, because of their higher concentration, they become closer to each other and/or form clusters. Concentration quenching is a well documented phenomenon where, as has been shown before, the emission from the Eu^{3+} ions in GaN was increasingly quenched in samples that contained Eu^{3+} concentrations of more than 2 at. % [99]. Note that in this last cited paper, the research team compared samples with 0.1, 2, 5 and 16 at.% of Eu^{3+} ions.

The FWHM of the 621 nm peaks in figure 4.6 is about 2.2 nm and presents constancy for the various Eu^{3+} concentrations. The data shown here is consistent with energy transfer processes (not the type of transfer described in chapter 2), and is further investigated in the following section. Nevertheless, the photoluminescence spectra shown in figure 4.6 agrees well with published literature on the subject where, for example, the energy transfer was confirmed by techniques such as photoluminescence excitation (PLE) [100] and Fourier transform infrared spectroscopy [101].

Cathodoluminescence measurements were also performed on the 1 at.% sample at room temperature. The excitation source used was a 3 keV electron beam focused to a spot of about 5 mm in diameter. The emission was measured using an Acton Research Corporation monochromator (model VM504) with both the input and output slits set at 500 μm . A Hamamatsu F2763 photomultiplier tube was used. Figure 4.7 shows the resulting spectrum. The bandedge emission and the 621 nm line are clearly visible. The FWHM of the 621 and 366 peaks are 1.6 and 14.2 nm respectively. The figure also shows many sharp transitions which were repeatable in samples that had different Eu^{3+} concentrations. Some of the peaks are attributed to known transitions as indicated on the graph. Other smaller non identified peaks on the spectrum are believed to be transitions from other 5D_j to 7F_j levels. Further studies on these peaks can provide much information on the energy transfer processes that go on between the host material (GaN) and the RE ions.

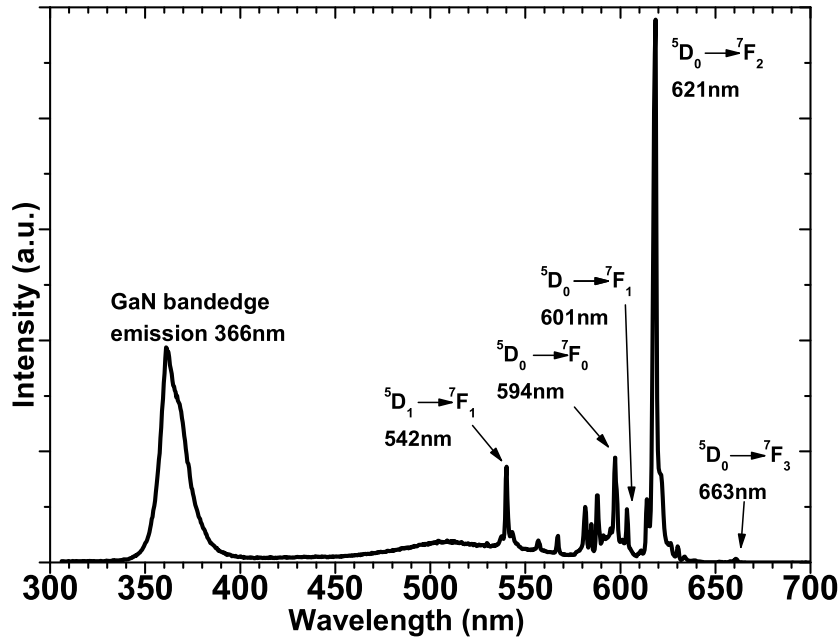


Figure 4.7. Room temperature cathodoluminescence of the GaN powder doped with a concentration of Eu^{3+} ions of 1 at.% (from [90]).

4.3.1 Lifetime Dynamics and Waveguide Application

Lifetime Dynamics of the Eu Doped GaN Powder

In order to compare the photoluminescence dynamics of our europium doped powder to other known dynamics of the same material obtained by more conventional methods (MBE), and to provide more insight into the quality of the material time resolved photoluminescence (TRPL) analyses were performed, as reported in [93]. A sample was prepared using a cellulose mixed with 1 at.% europium doped GaN powder which was spin coated onto a silicon substrate, resulting in a film of a few μm thick. As described before, the cellulose was baked off with a moderate temperature (450 C) anneal. The points of performing (temperature dependent)

lifetime measurements on the Eu doped GaN powder is to quantify the efficiency of the emission of the powder and to compare the lifetime parameters to existing values for the MBE grown GaN powder [98].

The TRPL measurements were performed on the 621 nm emission line of the 1 at.% europium doped powder. A pulsed N₂ laser (337.1 nm) with <4 ns pulse width, at a repetition rate of 29 Hz and pulse energy of approximately 2 μJ/cm² was used to measure the lifetime decays of the sample. The signals were measured with a spectral window of 4.5 meV centered on the 621 nm line using a photomultiplier tube. For temperature characterizations, a liquid nitrogen cooled cryostat was used for the measurements, from 80 K to room temperature.

Figure 4.8 shows one such lifetime decay curve of the sample. The lifetime decay curves all fit extremely well to a double exponential model of the form

$$A_S e^{-t/\tau_S} + A_F e^{-t/\tau_F}, \quad (4.1)$$

where the subscripts S and F refer to the slow and fast components of the decay. The logarithmic scale of the ordinate in figure 4.8 enhances the fact that the emitter initially undergoes a fast decay on the order of a few tens of microseconds, followed by a slower decay on the order of a few hundred microseconds. The faster decay component is associated with additional nonradiative decays to those of the slower component, the latter involving temperature insensitive radiative and temperature sensitive nonradiative decays [98, 100].

Figure 4.9 shows the temperature dependence of the slow (top of figure) and fast (bottom of figure) lifetime components of the best double exponential fits (see equation 4.1) to the TRPL decay curves of the europium doped GaN powder. A clear increase of both of the lifetime components as the temperature is reduced is obvious, indicating that at higher temperatures, nonradiative decay mechanisms

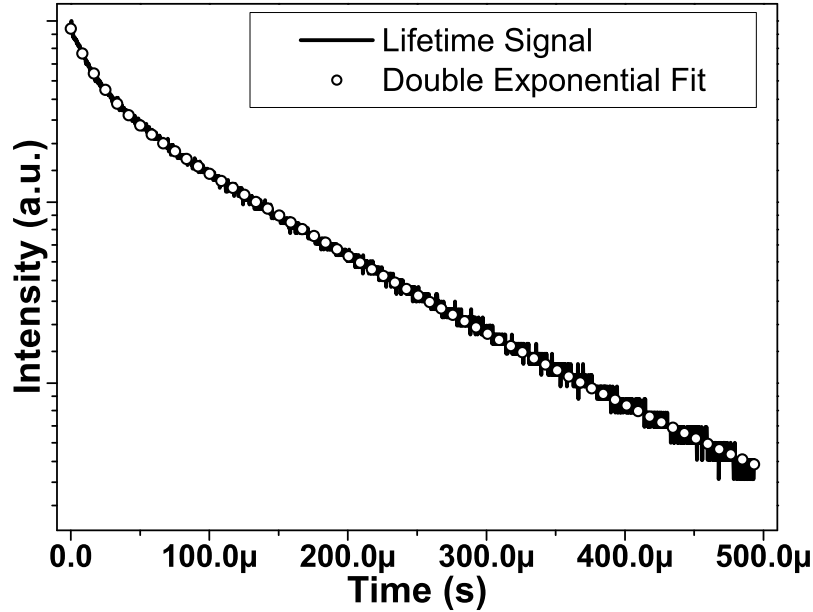


Figure 4.8. Lifetime decay curve (solid line) and double exponential fit (circles) of the 621 nm line of the Eu doped GaN powder (from [93]).

clearly affect the decay of the Eu^{3+} ions. When compared to previously published TRPL data of MBE grown Eu doped GaN [98], the present results have room temperature slow and fast lifetime components of approximately $\sim 253 \mu\text{s}$ and $18 \mu\text{s}$ respectively, while the reference [98] has results of $\sim 200 \mu\text{s}$ and $35 \mu\text{s}$ respectively. It is possible that there could be slight RE ion concentration differences between our GaN:Eu powder and the material used in reference [98]. Such small variations certainly affect the strength of the emission of the RE ions [90] through cross relaxation mechanisms, and it is expected that this would directly affect the lifetimes.

Close inspection of figure 4.9 reveals that there are two temperatures at which the behavior of the lifetime components changes, one at 185 K (corresponding

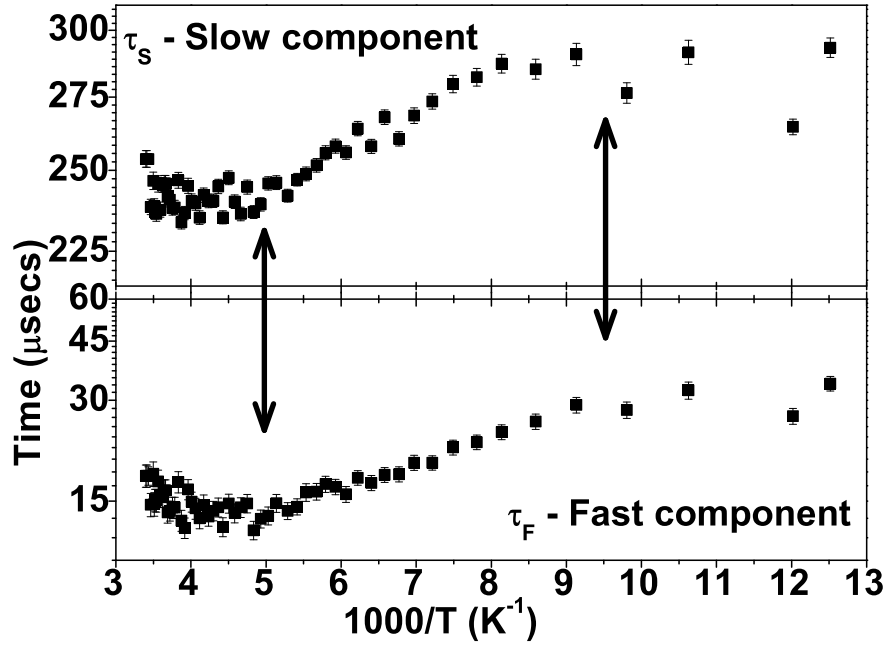


Figure 4.9. Temperature dependence of the lifetimes as a function of temperature obtained from best fits of equation 4.1 to the time decay curves from TRPL of the europium doped GaN powder. The two arrows indicate the temperatures at which the lifetime components undergo a change, one at 185 K and the other at 104 K (from [93]).

activation energy of 16 meV) and the other at 104 K (activation energy of 9 meV). Logarithmic ordinates were used in order to better reveal those two transition points. These changes signify that there may be two impurity levels below the GaN bandgap which contribute to the emission of the Eu ions, each positioned at 16 meV and 9 meV above 5D_0 . The role of these trap levels becomes clearer in the following pages with a better model to simulate the underlying excitation and relaxation processes.

A. J. Steckl, J. M. Zavada *et al.* reported not too long ago on the modeling of

the energy transfer and relaxation (i.e. emission from the RE ions) mechanisms of Eu doped GaN [98]. This model was developed in order to characterize the various processes that go on between the host material (GaN), the RE ions (Eu) and an impurity/trap present in the host. The reason for the existence of the latter is the fact that the double exponential modeling such as that used in equation 4.1 means that the RE ions must be exchanging excitation energy via nonradiative paths. It is possible that this impurity/trap be an internal state of the Eu ions for example, such as multipolar interactions between the RE ions [98].

Several models were considered in [98] and the one which best fitted the experimental data was kept. That same model is used here, and is shown in figure 4.10. For simplicity, the same nomenclature for identifying the various lifetime parameters is used as that found in [98]. The model shows the various excitation pathways between the host material (GaN), the Eu ions and the impurity/trap. The energy transfer between the host and the RE ions is characterized by a rate constant τ_{HE} . The interaction between the Eu ions and the impurity is modeled by two constants τ_{IE} and τ_{EI} , and the decay (emission) of the excited RE ions happens at a constant τ_{Decay} .²

The rate equations which describe the model shown in figure 4.10 are as follows

$$\begin{aligned} \frac{dN_{host}}{dt} &= g - \frac{1}{\tau_{HE}}N_{host}, \\ \frac{dN_{trap}}{dt} &= -\frac{1}{\tau_{IE}}N_{trap} + \frac{1}{\tau_{EI}}N_{Eu}, \\ \frac{dN_{Eu}}{dt} &= \frac{1}{\tau_{HE}}N_{host} + \frac{1}{\tau_{IE}}N_{trap} - \left(\frac{1}{\tau_{decay}} + \frac{1}{\tau_{EI}} \right) N_{Eu}, \end{aligned} \quad (4.2)$$

where g is the exciton generation rate, N_{host} is the number of excitons in the host

²For a more thorough discussion of the various excitation and relaxation time constants and their origins, a nice overview is presented in [98].

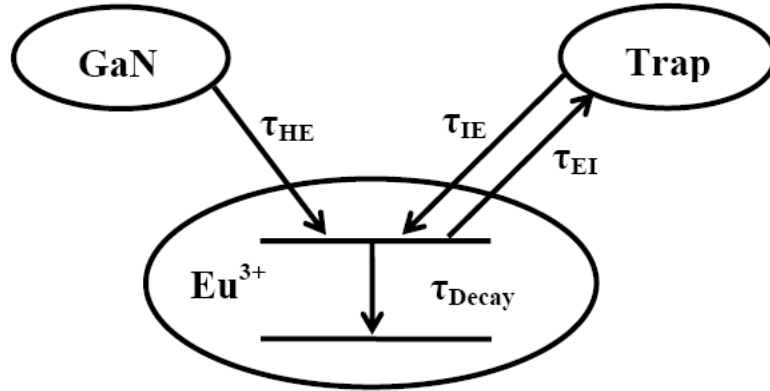


Figure 4.10. Schematic of the excitation and energy transfer processes model used for GaN:Eu (from [98]).

material (GaN), N_{trap} is the number of excitons in the impurity, and N_{Eu} is the number of excited Eu ions.

The differential equations shown in equations 4.2 were solved numerically by fitting them to the experimental data taken at various temperatures as described on page 57. Minimization of the χ^2 function was accomplished in order to get best fittings. An implementation of an explicit Runge-Kutta method was used in MATLAB to solve the differential equations.³ Since pulsed excitation was used for the measurements, g was set to 0, and the initial conditions (at $t = 0$) were $N_{host} = 1$, $N_{trap} = N_{Eu} = 0$. In other words, the instant $t = 0$ is when the pulse is assumed to have excited the host material (GaN), and the other processes with time constants τ_{HE} , τ_{IE} , τ_{EI} and τ_{decay} evolve from that instant.

Figure 4.11 shows the four lifetime parameters as a function of temperature. The first parameter, shown in figure 4.11(a), shows little variation with temperature except at the higher temperatures and is much slower than the recombination rate of excitons in GaN [102]. The rapidity of the transfer of energy between host

³The function `ode23` was used. For more information, see the MATLAB online help.

and RE ions is attributed to the fact that the Auger processes by which the excitons are transferred to the Eu ions are fast. The small variation with temperature of τ_{HE} would be the result of the fact that the transfer of energy to the RE ions easily excites the RE ions within the 5D_J manifold, and that there would be a "bottleneck" above the 5D_0 level (possibly a forbidden transition) which prevents τ_{HE} from being temperature sensitive [98]. Figure 4.11(b) shows the lifetime decay constant for the emission of the Eu at 621 nm. The logarithmic scale on the ordinate render the two clear transition points where the behavior of τ_{decay} changes easier to see, as was shown in figure 4.9, one at 185 K and the other at 104 K. It is interesting to note here that values for τ_{decay} are much different than the values shown in figure 4.9. The values for τ_S and τ_F in equation 4.1 represent some sort of composite of the underlying mechanisms of the decay of the excited Eu ions, on which more light is shed with the model adopted here. This will be discussed in more detail below in relation to the equations 4.2.

Lastly, figure 4.11(c) shows the two lifetime components responsible for transfer of energy between the Eu ions and the trap level. Clearly, the transfer of energy from the impurity to the Eu ions is relatively temperature independent, while the transfer of energy from the Eu ions to the impurity accelerates with increasing temperature. τ_{IE} , which models the backtransfer process from the impurity to the RE ions, is associated with nonresonant Auger scattering in conjunction with multiphonon emission and/or absorption [103]. Again on figure 4.11(c), the logarithmic y scale shows the two transition points where the behavior of both of the lifetime parameters changes, revealing again activation energies of 16 meV (185 K) and 9 meV (104 K). Note that the curve for τ_{EI} shows a much more pronounced increase with lower temperatures than τ_{IE} ; the logarithmic y scale appears to reduce that

effect.

It appears that, according to the previous model, the emission of the Eu ions in the GaN powder is more complex than a double exponential as that of equation 4.1. It turns out that the equations 4.2 can indeed be solved analytically. The interest here lies in the fact that for the decay of the Eu ions we will obtain a sum of three exponentials, with one of them having a fast time component, essentially leaving two exponentials. These two exponentials will have much complicated time arguments.

The equation for N_{host} in 4.2 is easily solved in our case. Using the initial condition that $N_{host}(t = 0) = 1$, we get that

$$N_{host}(t) = e^{-t/\tau_{HE}}. \quad (4.3)$$

The time derivative of the equation for N_{Eu} can be calculated, revealing a second order differential equation in which the equation for N_{trap} in 4.2 can be inserted. This gives the following

$$\frac{d^2 N_{Eu}}{dt^2} + \left(\frac{1}{\tau_{decay}} + \frac{1}{\tau_{EI}} + \frac{1}{\tau_{IE}} \right) \frac{dN_{Eu}}{dt} + \frac{N_{Eu}}{\tau_{IE}\tau_{decay}} = \left(\frac{1}{\tau_{IE}\tau_{HE}} - \frac{1}{\tau_{HE}^2} \right) e^{-t/\tau_{HE}}. \quad (4.4)$$

In order to simplify things, we use the following substitutions

$$\begin{aligned} A &= \frac{1}{\tau_{decay}} + \frac{1}{\tau_{EI}} + \frac{1}{\tau_{IE}} \\ B &= \frac{1}{\tau_{IE}\tau_{decay}} \\ C &= \frac{1}{\tau_{IE}\tau_{HE}} - \frac{1}{\tau_{HE}^2}. \end{aligned} \quad (4.5)$$

The homogenous solution to the second order equation 4.4 is of the following form

$$N_{Eu_h}(t) = C_1 e^{r_1 t} + C_2 e^{r_2 t}, \quad (4.6)$$

where

$$r_{1,2} = \frac{-A \pm \sqrt{A^2 - 4B}}{2}. \quad (4.7)$$

Combining equation 4.6 with the particular solution to equation 4.4, we get

$$N_{Eu}(t) = C_1 e^{r_1 t} + C_2 e^{r_2 t} + D e^{-t/\tau_{HE}}, \quad (4.8)$$

where

$$D = \frac{C}{\frac{1}{\tau_{HE}^2} - \frac{A}{\tau_{HE}} + B}. \quad (4.9)$$

As can be seen in equation 4.8, the decay of the excited Eu ions follows in fact three exponentials. However, the last exponential contains only a relatively fast component (τ_{HE}) with respect to the other two exponentials which have relatively slower components. Explicitly, the terms r_1 and r_2 can be written as

$$r_{1,2} = \frac{1}{2\tau_{Decay}\tau_{EI}\tau_{IE}} \left(\tau_{EI}\tau_{IE} + \tau_{Decay}(\tau_{EI} + \tau_{IE}) \pm \dots \right. \quad (4.10)$$

$$\left. \sqrt{\tau_{Decay}^2\tau_{EI}^2 + 2\tau_{Decay}\tau_{IE}\tau_{EI}(\tau_{Decay} - \tau_{EI}) + (\tau_{Decay} + \tau_{EI}^2\tau_{IE}^2)} \right).$$

Clearly, even though a double exponential fit as that used in equation 4.1 does provide good results, the two lifetime parameters τ_S and τ_F of that same equation actually reflect a rather complicated mix of the various lifetime parameters of our model. There is good agreement when comparing the parameters $r_{1,2}$ in equation 4.8 to the parameters τ_S and τ_F of equation 4.1 albeit with some error. This is attributed to the fact that the differential equations 4.2 were solved using a differential equation solver in MATLAB which has some level of uncertainty (see page 61).

Waveguide Application of the Eu Doped GaN Powder

A distinct advantage of the powder form of RE doped GaN compared to a substrate dependent MBE grown (for example) similar material is that it can be easily used

as a coating material. This results in effectively rendering optical properties using the active material to optically inert materials. The recent demonstration of a laser in silicon waveguides using a vertically offset active layer of AlGaInAs quantum wells shows the promise of the heterogenous combination [104].

We used a cellulose GaN:Eu dispersion to spin-coat a thin layer of the powder material onto SiON waveguides which guide visible light. The waveguides were fabricated on a silicon wafer on which a $5\ \mu\text{m}$ SiO₂ optical buffer layer was deposited using a plasma enhanced chemical vapor deposition (PECVD) tool. The GSI PECVD tool in the CNF cleanroom was used with the following specifications for the SiO₂ film: N₂, SiH₄ and N₂O gas flows at 1800, 18 and 1800 SCCM's respectively, 50W of RF power and a substrate temperature of 400 C. On top of the SiO₂ layer, a 700 nm layer of PECVD SiON was deposited also using the GSI PECVD tool. The specifications for the SiON layer were as follows: N₂, SiH₄, NH₃ and N₂O gas flows at 400, 40, 1900 and 700 SCCM's respectively, 250 W of RF power and a substrate temperature of 400 C. The waveguides were then patterned into this SiON layer using standard photolithography techniques, where OIR-620-7i photoresist was spun coated onto the wafer and exposed using a 5X GCA-6300 stepper tool. Reactive ion etching (RIE) was then used to etch away the unwanted SiON to leave behind the waveguides. The leftover photoresist is then removed using an oxygen plasma.

Figure 4.12 shows a cross-section of an SiON waveguide along with the simulated transverse electric (TE) fundamental modes at 621 nm (TE: electric field aligned in the left-right direction). The mode profiles in figure 4.12 were obtained using BeamPROPTM with the Correlation Method option [105]. An index of refraction of $n = 1.53$ was used for the SiON material. In figure 4.12(a), the mode

shown is that for the SiON waveguide only. Figure 4.12(b) shows the fundamental mode of the waveguide with a thin layer (100 nm) of the GaN:Eu powder, here assumed uniformly coating the waveguide.

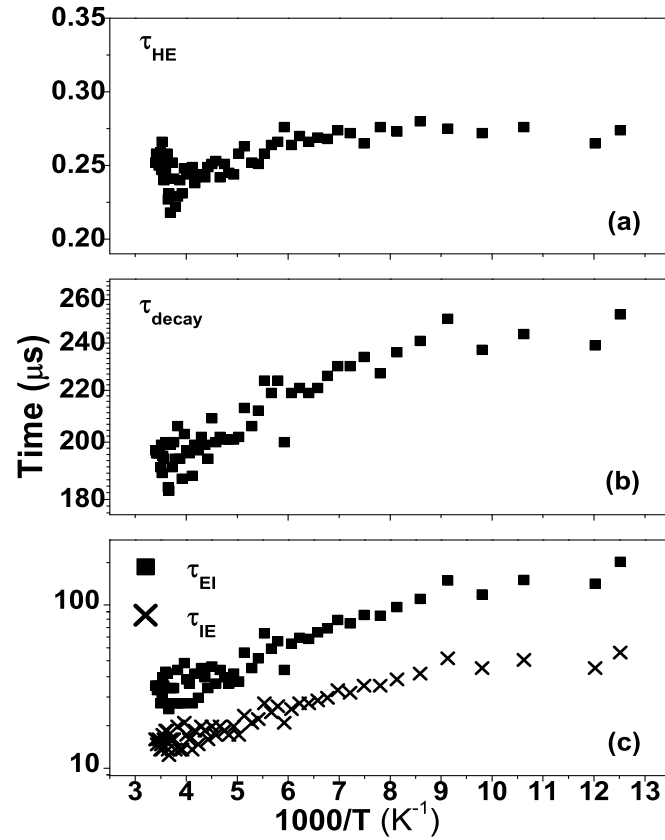


Figure 4.11. Time decay parameters obtained by best fits of the differential equations 4.2 to the lifetime measurements on the 621 nm line of the Eu doped GaN powder. (a) Energy transfer constant from the host (GaN) to the Eu ions. (b) Decay constant of the Eu ions at 621 nm. (c) Decay constants from the Eu ions to the trap (τ_{EI}) and from the trap to the Eu ions (τ_{IE}).

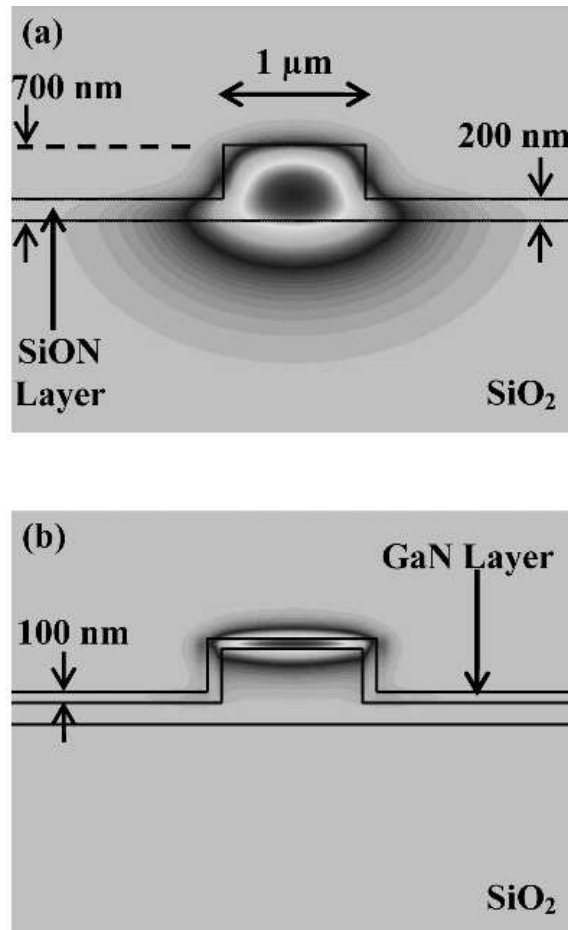


Figure 4.12. Schematic cross-section of an SiON waveguide along with the simulated TE fundamental mode at 621 nm. (a) TE mode of the SiON waveguide only, assuming $n = 1.53$. (b) TE mode in the GaN film which coats the waveguides, assuming $n = 1.53$ for the SiON and $n = 2.3$ for the GaN powder (from [93]).

Measurements of several SiON waveguides (without the GaN:Eu powder) with lengths varying from 3.9 mm to 7.7 mm resulted in propagation losses on the order of 26 dB/cm. The measurements were performed using the 457.9 nm line from an argon laser coupled into a single mode visible optical fiber. 300 μ W of power was measured at the tapered end of the optical fiber. This tapered end of the fiber was used to couple the laser light into the waveguides of the polished sample. The output of the waveguides was collected using an objective lens (0.55 NA) and sent onto a visible detector (Newport 818-SL). The presence of the GaN:Eu powder resulted in an increase of the propagation losses by approximately 8 ± 2 dB/cm. An improvement of the performance of this type of structure involves a post fabrication anneal performed on the SiON waveguides which is expected to greatly reduce propagation losses in the structure [106]. With reduced losses in the waveguides and improved coating processes with a powder consisting of small particulates, it is expected it would be possible to couple light emitted from the Eu (RE) doped GaN material into the waveguides.

CHAPTER 5

APPLICATIONS OF FLUORESCING CORE-SHELL SILICA NANOPARTICLES (CU DOTS)

5.1 Introduction

Integrated optics requires the use of light emitters (active materials), and the possibility of hybrid type structures, as outlined throughout this dissertation, is important so that their use on multiples platforms is achievable. Bright light emitters make them easier to work with, and fluorescing core-shell silica nanoparticles fall into this category.

As was recently reported, a class of highly fluorescent nanoparticles consisting of a fluorophore-rich "nucleus" surrounded with silica was developed [107]. These particles are essentially composed of a dye-rich center which is chemically reacted to be attached to silica to form the core, and this core is further encapsulated by doing a co-condensation with sol-gel precursor [107]. In the case of tetramethylrhodamine isothiocyanate (TRITC) dyes and 15 nm CU dots, the latter exhibit a brightness increased by a factor of 30 compared to the former. Photobleaching is also improved in the case of CU dots.

5.2 Experiments and Results

Two sets of experiments were performed on the CU dots [108]. The first one involved their insertion into a 1D microcavity, in a similar manner as was discussed in chapter 1, in order to control the emission of the CU dots. Figure 5.1 shows the photoluminescence spectrum of the CU dots that were used in the experiments. The 457.9 nm laser line of an argon laser was used as excitation. The central

wavelength of the emission spectrum is at 575 nm, which determines the thicknesses of the layers that will comprise the DBRs used for the microcavity. The microcavity structure was formed as described on page 15, with the exception that the thicknesses of the layers were $575/4n$ nm.

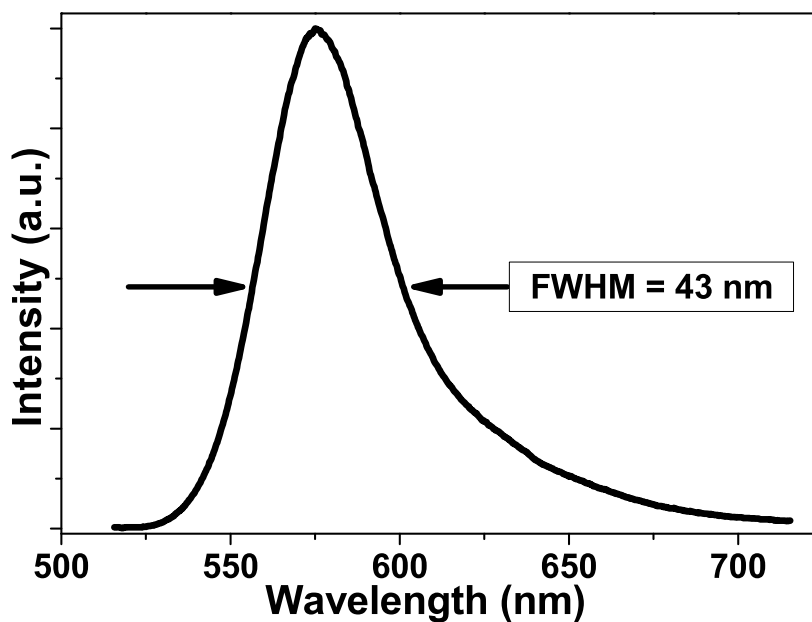


Figure 5.1. Photoluminescence spectrum of the TRITC CU Dots used in the experiments. The 457.9 nm laser line of an Argon laser was used for the excitation.

Figure 5.2 shows PL spectra of the CU dots from within the microcavity measured at three different positions on the sample. The measurements were performed using approximately 50 mW of CW laser light at 457.9 nm. Several points are worth noting here. The first one is the fact that the CU dots survived the fabrication processing involved in making the microcavity (i.e. the sputtering, which reaches temperatures of about 140 C as previously noted on page 16. This is quite interesting since the CU dots are comprised of an organic dye, which are usually

sensitive to temperature increases.

The second point worth mentioning with regard to figure 5.2 is the fact that, even though the FWHM of the emission from within the microcavity is reduced by a factor of about 4, the FWHM of the spectra are relatively larger than the expected FWHM for a comparable cavity (see page 18). This is attributed to the possibility that the absorption of the CU dots is altered due to the microcavity. Although no quantitative analyses have been performed (partly because of the third point discussed in the following paragraph), it is believed that, as discussed on page 18), the cavity enhances the absorption of the CU dots, possibly more significantly than the CdSe quantum dots. Further experiments would help understand the origin of this possible increase in absorption.

The last point, maybe the most important one, with regard to figure 5.2 has to do with the effect that the strong field inside the microcavity has on the life of the CU dots embedded in it. The spectra in figure 5.2 were measured using a monochromator with a scanning speed of 300 Å/min, which means that the about 3 minutes were necessary in order to measure an entire spectrum. Within this time, since the field inside the cavity is much stronger than the incident light that is impinging on it (for example, in a simple model of two mirrors with reflectivities of 99% that form a microcavity, the intensity upon one of the mirrors inside the microcavity is 100 times larger than the intensity that is impinging on the system [109], p. 149), the CU dots actually "die", gradually losing their intensity with time.

Figure 5.3 below shows the decay of the luminescence signal emitted from the CU dots from within the microcavity when 34 mW of CW laser light at 457.9 nm impinges on the microcavity to excite the CU dots. A double exponential

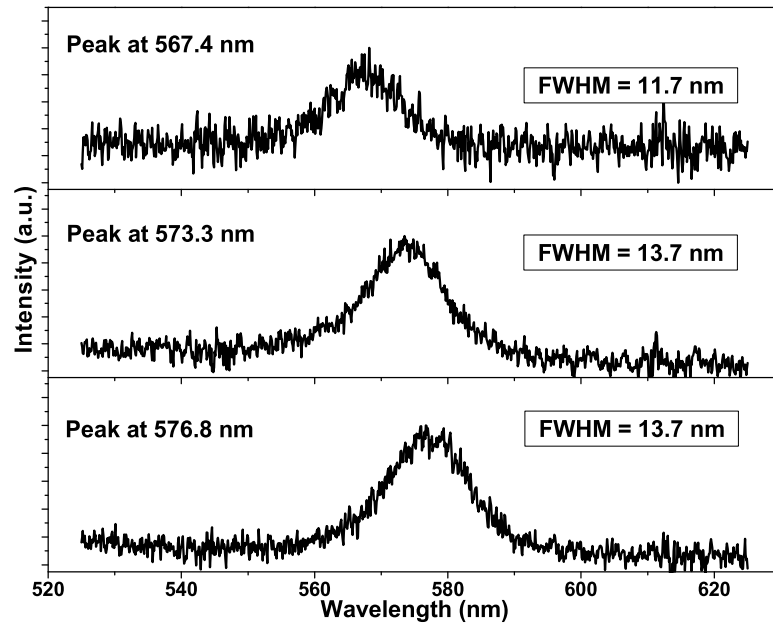


Figure 5.2. Photoluminescence spectra of the TRITC CU Dots from within the microcavity. Three spectra are shown as taken from three different positions on the sample.

fits well the decay of the signal, giving the following two values for the fast and slow "regimes" of the decay of the photoluminescence of the CU dots: 11.7 ± 0.3 and 112.8 ± 2.1 seconds. Within 21 seconds of exciting the sample with the Ar laser light, the intensity of the emission coming out of the microcavity is already reduced by half. In light of this, the PL spectra as shown in figure 5.2 are actually averages over 3 minutes of relatively rapidly decaying intensities. For this reason, it is difficult to quantify using CW excitation whether or not enhancement of the luminescence of the CU dots is present. The fact that the time decay of the luminescence signals of the CU dots from within the microcavity does not necessarily mean that the mechanisms responsible for this decay and the intensity

of the resulting signal coming out of the microcavity are simple. Several effects are at work such as the actual destruction of the CU dots (photobleaching, deeper changes in the chemistry of the dyes) and the ensuing changes in the absorption and emission properties of the material inside the microcavity.

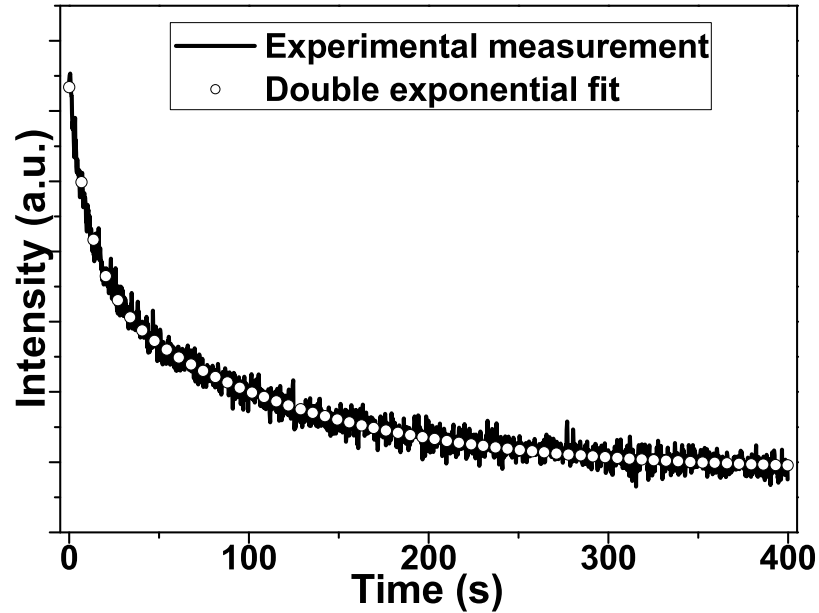


Figure 5.3. Time decay of the photoluminescence of the CU dots from within the microcavity (on resonance) The graph shows the experimental measurements (solid line) as well as a double exponential fit (open circles).

The second experiment which was performed using the CU dots was done using SiON waveguides similar to those described on page 66. Although qualitative at this stage, this experiment shows the promise of using a light emitter such as the CU dots for display applications. Visible light guiding SiON waveguides were fabricated and CU dots were placed on the surface of the die. A small drop of the CU dots solution (in ethanol) placed on a small portion of one of the SiON

waveguides was simply allowed to dry so that only the CU dots remained once the solvent was evaporated. The 457.9 nm laser light of an argon laser was coupled into the waveguide using a tapered visible optical fiber. The light propagating in the waveguide excited the CU dots in the region where the latter were in contact with the waveguide. Figure 5.4(a) shows a photograph of the chip mounted in the optical setup used in the laboratory. To the right of the chip is an optical fiber which guides the Ar laser light and couples this light into one of the waveguides on the chip. The guiding of this light by the waveguide is apparent on the photograph. Figure 5.4(b) is a picture taken of the same optical setup as shown in figure 5.4(a) but with a filter to prevent the laser light from entering the camera. The excitation of the CU dots is apparent from figure 5.4(b) where only the portion where the CU dots were deposited is visible from their glow as a result of the laser light being guided in the waveguide. This shows the promise of using CU dots as light emitters for displays and possibly as phosphors.

Applications of CU dots appear to be most promising for labeling and sensing (as is already done with uncapped dyes). The silica cladding, which encapsulates the dye core, renders the CU dots ideal candidates for biological applications since conjugation chemistry can be easily performed on them. Their ease of use make them appealing candidates since a simple spin coating technique can be used. Placing CU dots in a microcavity and exciting them optically has resulted in their degradation, as shown in figure 5.3, as a result of the more intense radiation field where the CU dots are located.

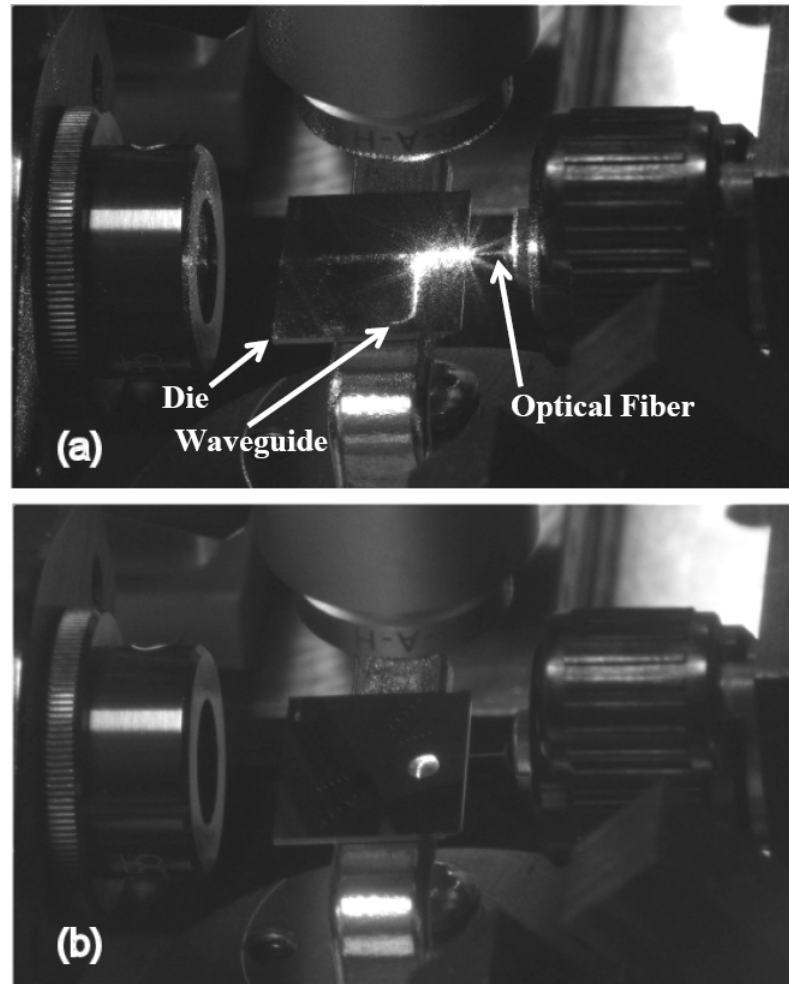


Figure 5.4. Pictures of Ar laser light at 457.9 nm guided in an SiON waveguide with CU dots on top of the waveguide. The pictures were taken (a) without any filtering, showing the guiding of the laser light, and (b) with filtering in order to prevent the Ar light from entering the camera, revealing the glowing CU dots.

APPENDIX A

**EVALUATION OF THE GREEN FUNCTION IN THE QED
TREATMENT OF FRET**

This appendix discusses the evaluation of the Green function integral obtained in equation 3.24

$$G(k, R) = \int_{-\infty}^{\infty} \frac{\sin pR}{2R} \left\{ \frac{1}{k-p} + \frac{1}{-k-p} \right\} dp. \quad (\text{A.1})$$

While the result (and not the actual calculations) of this last integral is presented in published articles (see for example [54, 55]), the intent of the present discussion is to underline the fact mathematical calculations, even though correct, do not necessarily lead to the final correct result.

Although equation A.1 is reminiscent of the Helmholtz equation (the Green function does, after all, satisfy the Helmholtz equation, $-(\nabla^2 + k^2)G = \delta(\mathbf{R})$ - see for example [110]), the same reasonings of classical electrodynamics, for example, to solve the Helmholtz equation, i.e. that the solution (a harmonic solution) be the result of a localized source in a finite region of space, does not apply to QED. Indeed, the classical picture (even in semi-classical modeling) easily allows for the "visualization" of an outgoing wavefront as in figure 3.1(a) on page 33, where the path of energy transfer is shown for the initially excited donor first losing its energy which is then transferred over to the acceptor. However, for the case as shown in figure 3.1(b), which must be included in the QED description, this same type of "visualization" does not apply. It is for this reason that equation A.1 must be solved by keeping in mind the above discussion. Ultimately, this must lead a solution for the Green function which agrees with the well-proven Förster result for energy transfer.

Equation A.1 can be rewritten as

$$G(k, R) = \frac{i}{2R} \int_{-\infty}^{\infty} \frac{e^{ipR} - e^{-ipR}}{(p-k)(p+k)} p dp. \quad (\text{A.2})$$

This last equation can be evaluated by contour integration, but care must be taken with regard to which contour is to be used. There are in fact several contours in the complex plane that can be used to solve equation A.2, and the appropriate one is shown in figure A.1 (for the e^{ipR} term). A similar contour is used to solve for the e^{-ipR} term with the exception that the semicircle will close to $-\infty$. Other contours will lead to unreasonable solutions that go against the discussion presented in the previous paragraph, as shown in [54] for example.

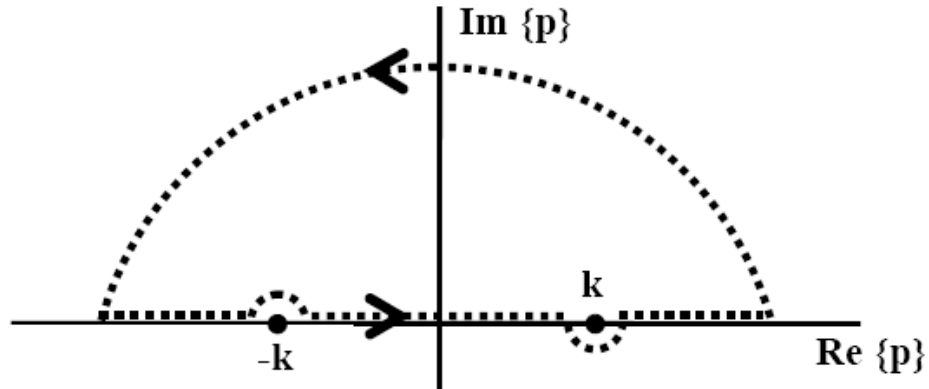


Figure A.1. Adequate contour for the integration of equation A.1 (for the e^{ipR} term).

We will first solve the e^{ipR} integral in equation A.2. This integral can be written as the sum of four integrals

$$\begin{aligned} I_1 &= \frac{i}{2R} \int_{-\infty}^{\infty} \frac{e^{ipR}}{(p-k)(p+k)} p dp \\ &= - \int_{\text{Semicircle}} - \int_{\text{Pole } p=-k} - \int_{\text{Pole } p=k} + \text{Residue Integral} \\ &= -I_A - I_B - I_C + I_D. \end{aligned} \quad (\text{A.3})$$

The first integral in equation A.3 is for the semicircle going to infinity. To solve it, we can make the substitution $p = re^{i\theta} \rightarrow dp = i\theta re^{i\theta} d\theta$, giving

$$\begin{aligned} I_A &= \frac{i}{2R} \lim_{r \rightarrow \infty} \int_0^\pi \frac{ir^2 e^{2i\theta} e^{iRr \cos \theta} e^{-Rr \sin \theta}}{(re^{i\theta} - k)(re^{i\theta} + k)} d\theta \\ &\sim \frac{i}{2R} \lim_{r \rightarrow \infty} \int_0^\pi e^{-Rr \sin \theta}, \end{aligned} \quad (\text{A.4})$$

where the last is simply the result of Jordan's lemma.¹ The purpose of doing this integral is to ensure that the integral over the semicircle going to infinity has a finite value, and this is clearly the case as shown in the last equation, which is equal to 0. Care must be taken though since R does vary in our problem. Recalling that R represents the distance between the donor and acceptor, the last equation obviously converges to 0 as $R \rightarrow \infty$. However, if $R \rightarrow 0$, this signifies that there is no separation between donor and acceptor, and there is no longer "physicality" to our problem. Therefore, the case where $R \rightarrow 0$ is of no concern (as is also obvious in the final answer for $G(k, R)$ which diverges for $R \rightarrow 0$).

The second integral I_B in equation A.3 is solved by making the substitution $p + k = \epsilon e^{i\theta} \rightarrow dp = i\epsilon e^{i\theta} d\theta$, giving

$$\begin{aligned} I_B &= \frac{i}{2R} \lim_{\epsilon \rightarrow 0} \int_\pi^0 i \frac{e^{iR(\epsilon e^{i\theta} - k)} (\epsilon e^{i\theta} - k)}{\epsilon e^{i\theta} (\epsilon e^{i\theta} - 2k)} d\theta \\ &= \frac{i}{2R} \int_\pi^0 i \frac{e^{-ikr}}{2} d\theta \\ &= \frac{\pi}{4R} e^{-ikr} \end{aligned} \quad (\text{A.5})$$

The third integral I_C in equation A.3 is solved in a similar way to I_B with the exception that the substitution $p - k = \epsilon e^{i\theta} \rightarrow dp = i\epsilon e^{i\theta} d\theta$ is used, and that the

¹Jordan's lemma in complex analysis is simply the result of the fact that the integral over the infinite semicircle of a definite integral of the type considered here goes to zero. See for example [111].

limits of integration now range from $\pi \rightarrow 2\pi$, giving the final result

$$I_C = -\frac{\pi}{4R} e^{ikr} \quad (\text{A.6})$$

Lastly, the fourth integral I_D is simply the integral using the residue theorem. Figure A.1 shows that since only the pole at $p = k$ is included in the contour, we have that

$$\begin{aligned} I_D &= \frac{i}{2R} \oint \frac{e^{ipR}}{(p-k)(p+k)} p \, dp \\ &= 2\pi i \sum \text{Residues} \\ &= -\frac{\pi}{R} \left(\frac{e^{ipR} p}{p+k} \right)_{p=k} \\ &= -\frac{\pi}{2R} e^{ikR}. \end{aligned} \quad (\text{A.7})$$

Putting all of the values together, we get that

$$I_1 = \frac{i}{2R} \int_{-\infty}^{\infty} \frac{e^{ipR}}{(p-k)(p+k)} p \, dp = -\frac{\pi}{2R} e^{ikr}. \quad (\text{A.8})$$

Similar calculations can be done to solve the e^{ipR} integral in equation A.2. With the semicircle in figure A.1 extending in the lower half plane, we also obtain

$$\frac{i}{2R} \int_{-\infty}^{\infty} \frac{e^{-ipR}}{(p-k)(p+k)} p \, dp = -\frac{\pi}{2R} e^{ikr}. \quad (\text{A.9})$$

With the values of the last two equations, we finally obtain

$$G(k, R) = -\frac{\pi}{R} e^{ikR}. \quad (\text{A.10})$$

Other contours than the one shown in figure A.1 are obviously possible, but their results are erroneous, giving a Green function that is $\sim (\cos kR)/R$. In the radiative limit of such an equation (i.e. for $kR \gg 1$), this results in value for the rate of energy transfer which goes as $\cos^2 kR$, i.e. an oscillating regime. Equation A.10 is indeed the correct result and, interestingly enough, is strikingly similar to

the classical electrodynamic result of a spherical wave (as solution to the Helmholtz equation).

In reference [54], the evaluation of the Green function is also performed a different way by rewriting the Green function and obtaining intermediary results of a cosine and a shifted sine integrals before getting the final result, equation A.10.

BIBLIOGRAPHY

- [1] M. Lipson, “Guiding, modulating, and emitting light on Silicon-challenges and opportunities”, *J. Lightwave Technol.*, Vol. 23, No. 12, pp. 4222–38, Dec. 2005.
- [2] C.A. Leatherdale, W.-K. Woo, F.V. Mikulec, and M.G. Bawendi, “On the absorption cross section of CdSe nanocrystal quantum dots”, *J. Phys. Chem. B*, Vol. 106, No. 31, pp. 7619–22, 08 Aug. 2002.
- [3] C. Murray, C. Kagan, and M.G. Bawendi, “Synthesis and Characterization of Monodisperse Nanocrystals and Close-Packed Nanocrystal Assemblies”, *Annu. Rev. Mater. Sci.*, Vol. 30, No. 546, 2000.
- [4] W.U. Huynh, J.J. Dittmer, and A.P. Alivisatos, “Hybrid nanorod-polymer solar cells”, *Science*, Vol. 295, No. 5564, pp. 2425–7, 29 March 2002.
- [5] V.I. Klimov, A.A. Mikhailovsky, S. Xu, A. Malko, J.A. Hollingsworth, C.A. Leatherdale, H.-J. Eisler, and M.G. Bawendi, “Optical gain and stimulated emission in nanocrystal quantum dots”, *Science*, Vol. 290, No. 5490, pp. 314–17, 13 Oct. 2000.
- [6] M. Kazes, D.Y. Lewis, Y. Ebenstein, T. Mokari, and U. Banin, “Lasing from semiconductor quantum rods in a cylindrical microcavity”, *Adv. Mater.*, Vol. 14, No. 4, pp. 317–321, 2002.
- [7] A.V. Malko, A.A. Mikhailovsky, M.A. Petruska, J.A. Hollingsworth, H. Htoon, M.G. Bawendi, and V.I. Klimov, “From amplified spontaneous emission to microring lasing using nanocrystal quantum dot solids”, *Appl. Phys. Lett.*, Vol. 81, No. 7, pp. 1303–5, 12 Aug. 2002.

- [8] J. Lee, V.C. Sundar, J.R. Heine, M.G. Bawendi, and K.F. Jensen, “Full color emission from II-VI semiconductor quantum dot-polymer composites”, *Adv. Mater.*, Vol. 12, No. 15, pp. 1102–5, 02 Aug. 2000.
- [9] N. Tessler, V. Medvedev, M. Kazes, ShiHai Kan, and U. Banin, “Efficient near-infrared polymer nanocrystal light-emitting diodes”, *Science*, Vol. 295, No. 5559, pp. 1506–8, 22 Feb. 2002.
- [10] R.E. Bailey, A.M. Smith, and S. Nie, “Quantum dots in biology and medicine”, *Physica E*, Vol. 25, No. 1, pp. 1–12, Oct. 2004.
- [11] M.V. Artemyev and U. Woggon, “Quantum dots in photonic dots”, *Appl. Phys. Lett.*, Vol. 76, No. 11, pp. 1353, 2000.
- [12] M.V. Artemyev, U. Woggon, and R. Wannemacher, “Photons confined in hollow microspheres”, *Appl. Phys. Lett.*, Vol. 78, No. 8, pp. 1032–1034, 2001.
- [13] X. Fan, M.C. Lonergan, Y. Zhang, and H. Wang, “Enhanced spontaneous emission from semiconductor nanocrystals embedded in whispering gallery optical microcavities”, *Phys. Rev. B*, Vol. 64, pp. 115310, 2001.
- [14] M.V. Artemyev, U. Woggon, R. Wannemacher, H. Jaschinski, and W. Langbein, “Light Trapped in a Photonic Dot: Microspheres Act as a Cavity for Quantum Dot Emission”, *Nano Lett.*, Vol. 1, No. 6, pp. 309–314, 2001.
- [15] Xudong Fan, Phedon Palinginis, Scott Lacey, Hailin Wang, and Mark C. Lonergan, “Coupling semiconductor nanocrystals to a fused-silica microsphere: A quantum-dot microcavity with extremely high Q factors”, *Opt. Lett.*, Vol. 25, No. 21, pp. 1600–1602, 2000.

- [16] T.D. Happ, I.I. Tartakovskii, V.D. Kulakovskii, J.-P. Reithmaier, M. Kamp, and A. Forchel, “Enhanced light emission of $\text{In}_x\text{Ga}_{1-x}\text{As}$ quantum dots in a two-dimensional photonic-crystal defect microcavity”, *Phys. Rev. B, Condens. Matter Mater. Phys.*, Vol. 66, No. 4, pp. 041303–1, 15 July 2002.
- [17] V Zwiller, N. Chitica, J. Persson, M.-E. Pistol, W. Seifert, L. Samuelson, M. Hammar, K. Streubel, E. Goobar, and G. Bjork, “Studies of self-assembled InP quantum dots in planar microcavities”, *Materials Science and Engineering B: Solid-State Materials for Advanced Technology*, Vol. 69, pp. 314–317, Jan. 2000.
- [18] E. Moreau, I. Robert, J.M. Gerard, I. Abram, L. Manin, and V. Thierry-Mieg, “Single-mode solid-state single photon source based on isolated quantum dots in pillar microcavities”, *Appl. Phys. Lett.*, Vol. 79, No. 18, pp. 2865–7, 29 Oct. 2001.
- [19] H. Yokoyama, K. Nishi, T. Anan, H. Yamada, S.D. Brorson, and E.P. Ippen, “Enhanced spontaneous emission from GaAs quantum wells in monolithic microcavities”, *Appl. Phys. Lett.*, Vol. 57, No. 26, pp. 2814–16, 24 Dec. 1990.
- [20] C.B. Murray, D.J. Norris, and M.G. Bawendi, “Synthesis and characterization of nearly monodisperse CdE (E = sulfur, selenium, tellurium) semiconductor nanocrystallites”, *J. Am. Chem. Soc.*, Vol. 115, No. 19, pp. 8706–15, 22 Sept. 1993.
- [21] L. Qu, Z.A. Peng, and X. Peng, “Alternative routes toward high quality CdSe nanocrystals”, *Nano Lett.*, Vol. 1, No. 6, pp. 333–7, June 2001.

- [22] Margaret A. Hines and Philippe Guyot-Sionnest, “Synthesis and characterization of strongly luminescing ZnS-capped CdSe nanocrystals”, *J. Phys. Chem.*, Vol. 100, No. 2, pp. 468–471, 11 Jan. 1996.
- [23] B.O. Dabbousi, J. Rodriguez-Viejo, F.V. Mikulec, J.R. Heine, H. Mattoussi, R. Ober, K.F. Jensen, and M.G. Bawendi, “(CdSe)ZnS core-shell quantum dots: Synthesis and characterization of a size series of highly luminescent nanocrystallites”, *J. Phys. Chem. B*, Vol. 101, No. 46, pp. 9463–9475, 13 Nov. 1997.
- [24] C.B. Poitras, M. Lipson, Hui Du, M.A. Hahn, and T.D. Krauss, “Photoluminescence enhancement of colloidal quantum dots embedded in a monolithic microcavity”, *Appl. Phys. Lett.*, Vol. 82, No. 23, pp. 4032–4, 09 Jun. 2003.
- [25] C.B. Poitras, M. Lipson, M.H. Hahn, H. Du, and T.D. Krauss, “Enhanced spontaneous emission from colloidal quantum dots embedded in a monolithic microcavity”, *Conference on Quantum Electronics and Laser Science (QEELS) - Technical Digest Series*, Vol. 89, pp. 5, 2003.
- [26] Lin-Wang Wang and A. Zunger, “Pseudopotential calculations of nanoscale CdSe quantum dots”, *Phys. Rev. B, Condens. Matter*, Vol. 53, No. 15, pp. 9579–82, 15 Apr. 1996.
- [27] A. Franceschetti and A. Zunger, “Optical transitions in charged CdSe quantum dots”, *Phys. Rev. B, Condens. Matter*, Vol. 62, No. 24, pp. 16287–90, 15 Dec. 2000.
- [28] Lin-Wang Wang, M. Califano, A. Zunger, and A. Franceschetti, “Pseudopo-

- tential theory of Auger processes in CdSe quantum dots”, *Phys. Rev. Lett.*, Vol. 91, No. 5, pp. 056404–1, 01 Aug. 2003.
- [29] H.H. von Grunberg, “Energy levels of CdSe quantum dots: Wurtzite versus zinc-blende structure”, *Phys. Rev. B, Condens. Matter*, Vol. 55, No. 4, pp. 2293–302, 15 Jan. 1997.
- [30] T. Takagahara, “Effects of dielectric confinement and electron-hole exchange interaction on excitonic states in semiconductor quantum dots”, *Phys. Rev. B, Condens. Matter*, Vol. 47, No. 8, pp. 4569–84, 15 Feb. 1993.
- [31] D. Patra, I. Gregor, J. Enderlein, and M. Sauer, “Defocused imaging of quantum-dot angular distribution of radiation”, *Appl. Phys. Lett.*, Vol. 87, No. 10, pp. 101103–1, 5 Sept. 2005.
- [32] J.D. Joannopoulos, R.D. Meade, and J.N. Winn, *Photonic Crystals: Molding the Flow of Light*, Princeton University Press, July 1995.
- [33] E. Hecht, *Optics*, Adidson Wesley Longman, Inc., New York, NY, 3rd edition, 1998.
- [34] W.G.J.H.M. van Sark, P.L.T.M. Frederix, D.J. van den Heuvel, A.A. Bol, J.N.J. van Lingen, C. de Mello Donega, H.C. Gerritsen, and A. Meijerink, “Time-resolved fluorescence spectroscopy study on the photophysical behavior of quantum dots”, *J. Fluoresc.*, Vol. 12, No. 1, pp. 69–76, March 2002.
- [35] R. Harel, E. Cohen, A. Ron, E. Linder, and L.N. Pfeiffer, “Magnetic-field-induced cavity polariton linewidth reduction in a GaAs/Al_{0.1}Ga_{0.9}As microcavity”, *Phys. Rev. B, Condens. Matter*, Vol. 60, No. 16, pp. 11550–6, 15 Oct. 1999.

- [36] E.F. Schubert, N.E.J. Hunt, R.J. Malik, M. Micovic, and D.L. Miller, “Temperature and modulation characteristics of resonant-cavity light-emitting diodes”, *J. Lightwave Technol.*, Vol. 14, No. 7, pp. 1721–9, July 1996.
- [37] R. Coccioli, M. Boroditsky, K.W. Kim, Y. Rahmat-Samii, and E. Yablono-
vitch, “Smallest possible electromagnetic mode volume in a dielectric cavity”,
IEE Proc., Optoelectron., Vol. 145, No. 6, pp. 391–7, Dec. 1998.
- [38] U. Woggon, R. Wannemacher, M.V. Artemyev, B. Moller, N. Lethomas,
V. Anikeyev, and O. Schops, “Dot-in-a-dot: Electronic and photonic con-
finement in all three dimensions”, *Applied Physics B: Lasers and Optics*,
Vol. 77, No. 5, pp. 469–484, 2003.
- [39] N. Le Thomas, U. Woggon, O. Schops, M.V. Artemyev, M. Kazes, and
U. Banin, “Cavity QED with semiconductor nanocrystals”, *Nano Lett.*,
Vol. 6, No. 3, pp. 557–561, 2006.
- [40] R. van Grondelle, .P. Dekker, T. Gillbro, and V. Sundstrom, “Energy transfer
and trapping in photosynthesis”, *Biochim. Biophys. Acta - Bioenergetics*,
Vol. 1187, No. 1, pp. 1–65, 1994.
- [41] X.C. Hu. and K. Schulten, “How nature harvests sunlight”, *Phys. Today*,
Vol. 50, pp. 28–34, 1997.
- [42] M.A. Baldo, M.E. Thompson, and S.R. Forrest, “High-efficiency fluorescent
organic light-emitting devices using a phosphorescent sensitizer”, *Nature*,
Vol. 403, No. 6771, pp. 750–3, 17 Feb. 2000.
- [43] A. Dodabalapur, L.J. Rothberg, R.H. Jordan, T.M. Miller, R.E. Slusher,

- and J.M. Phillips, “Physics and applications of organic microcavity light emitting diodes”, *J. Appl. Phys.*, Vol. 80, No. 12, 15 Dec. 1996.
- [44] C.R. Kagan, C.B. Murray, M. Nirmal, and M.G. Bawendi, “Electronic energy transfer in CdSe quantum dot solids”, *Phys. Rev. Lett.*, Vol. 76, No. 9, pp. 1517–20, 26 Feb. 1996.
- [45] C.E. Finlayson, D.S. Ginger, and N.C. Greenham, “Enhanced Forster energy transfer in organic/inorganic bilayer optical microcavities”, *Chem. Phys. Lett.*, Vol. 338, No. 2-3, pp. 83–7, 20 Apr. 2001.
- [46] A.R. Clapp, I.L. Medintz, J.M. Mauro, B.R. Fisher, M.G. Bawendi, and H. Mattoussi, “Fluorescence Resonance Energy Transfer between Quantum Dot Donors and Dye-Labeled Protein Acceptors”, *Jnl. Amer. Chem. Soc.*, Vol. 126, No. 1, pp. 301–310, 2004.
- [47] M. Achermann, M.A. Petruska, S. Kos, D.L. Smith, D.D. Koleske, and V.I. Klimov, “Energy-transfer pumping of semiconductor nanocrystals using an epitaxial quantum well”, *Nature*, Vol. 429, No. 6992, pp. 642–646, 2004.
- [48] T. Förster, “Intermolecular energy transference and fluorescence”, *Annalen der Physik*, Vol. 2, No. 1-2, pp. 55–75, 1948.
- [49] J.R. Lakowicz, *Principles of Fluorecence Spectroscopy*, Kluwer Academic/Plenum, New York, NY, 2nd edition, 1999, p. 367.
- [50] G.D. Scholes and D.L. Andrews, “Resonance energy transfer and quantum dots”, *Phys. Rev. B (Condens. Matter Mater. Phys.)*, Vol. 72, No. 12, pp. 125331–1, 15 Sept. 2005.

- [51] D.L. Andrews, “A unified theory of radiative and radiationless molecular energy transfer”, *Chem. Phys.*, Vol. 135, No. 2, pp. 195–201, 01 Aug. 1989.
- [52] D.P. Craig and T. Thirunamachandran, “An analysis of models for resonant transfer of excitation using quantum electrodynamics”, *Chem. Phys.*, Vol. 167, No. 3, pp. 229–240, 15 Nov. 1992.
- [53] G.D. Scholes and D.L. Andrews, “Damping and higher multipole effects in the quantum electrodynamical model for electronic energy transfer in the condensed phase”, *J. Chem. Phys.*, Vol. 107, No. 14, pp. 5374–84, 08 Oct. 1997.
- [54] G.J. Daniels, R.D. Jenkins, D.S. Bradshaw, and D.L. Andrews, “Resonance energy transfer: the unified theory revisited”, *J. Chem. Phys.*, Vol. 119, No. 4, pp. 2264–74, 22 July 2003.
- [55] David L. Andrews and David S. Bradshaw, “Virtual photons, dipole fields and energy transfer: A quantum electrodynamical approach”, *European Journal of Physics*, Vol. 25, No. 6, pp. 845–858, Nov. 2004.
- [56] D.L. Andrews and B.S. Sherborne, “Resonant excitation transfer: a quantum electrodynamical study”, *J. Chem. Phys.*, Vol. 86, No. 7, pp. 4011–17, 01 Apr. 1987.
- [57] D.L. Andrews, “A unified theory of radiative and radiationless molecular energy transfer”, *Chem. Phys.*, Vol. 135, No. 2, pp. 195–201, 01 Aug. 1989.
- [58] S.K. Sekatskii and G. Dietler, “Using Magnetic Dipole Transitions for Fluorescence Resonance Energy Transfer”, *Anal. Biochem.*, Vol. 299, No. 2, pp. 263–266, 15 Dec. 2001.

- [59] D.F. Walls and G.J. Milburn, *Quantum Optics*, Springer-Verlag New York, LLC, New York, NY, 2nd printing edition, 1995.
- [60] M.E. Peskin and D.V. Schroeder, *An Introduction to Quantum Field Theory*, Perseus Publishing, Jackson, TN, 1995.
- [61] N.W. Ashcroft and N.D. Mermin, *Solid State Physics*, Saunders College Publishing, Orlando, FL, 1976.
- [62] R. Loudon, *The Quantum Theory of Light*, Oxford University Press, New York, NY, 3rd edition, 2000.
- [63] D.L. Andrews and T. Thirunamachiandran, “On three-dimensional rotational averages”, *J. Chem. Phys.*, Vol. 67, No. 11, pp. 5026–33, 01 Dec. 1977.
- [64] G. Juzelinas and D.L. Andrews, “Quantum electrodynamics of resonance energy transfer”, *Adv. Chem. Phys.*, Vol. 112, pp. 357–410, 2000.
- [65] G. Juzeliunas and D.L. Andrews, “Quantum electrodynamics of resonant energy transfer in condensed matter”, *Phys. Rev. B, Condens. Matter*, Vol. 49, No. 13, pp. 8751–63, 01 Apr. 1994.
- [66] L. Guo, X. Teng, H. Yang, T.D. Krauss, C.B. Poitras, and M. Lipson, “Energy Transfer between Colloidal Semiconductor Nanocrystals in an Optical Microcavity”, *Appl. Phys. Lett.*, June 2006, submitted.
- [67] Z. Yu, L. Guo, H. Du, T. Krauss, and J. Silcox, “Shell Distribution on Colloidal CdSe/ZnS Quantum Dots”, *Nano Lett.*, Vol. 5, No. 4, pp. 565–70, 09 Mar. 2005.

- [68] M.J.A. de Dood, A. Polman, and J.G. Fleming, “Modified spontaneous emission from erbium-doped photonic layer-by-layer crystals”, *Phys. Rev. B*, Vol. 67, No. 11, pp. 115106, 2003.
- [69] H. Morkoc and S.N. Mohammad, “High-luminosity blue and blue-green gallium nitride light-emitting diodes”, *Science*, Vol. 267, No. 5194, pp. 51–5, 06 Jan. 1995.
- [70] T. Matsuoka, “InGaAlN and II-VI systems for blue-green light-emitting devices”, *Adv. Mater.*, Vol. 8, No. 6, pp. 469–79, June 1996.
- [71] A.J. Steckl and J.M. Zavada, “Optoelectronic properties and applications of rare-earth-doped GaN”, *MRS Bull.*, Vol. 24, No. 9, pp. 33–8, Sept. 1999.
- [72] A.J. Steckl, J. Heikenfeld, M. Garter, R. Birkhahn, and D.S. Lee, “Rare earth doped gallium nitride-light emission from ultraviolet to infrared”, *Compound Semicond.*, Vol. 6, No. 1, pp. 48–50, Jan. 2000.
- [73] A.J. Steckl, J.C. Heikenfeld, D.-S. Lee, M.J. Garter, C.C. Baker, Y. Wang, and R. Jones, “Rare-earth-doped GaN: growth, properties, and fabrication of electroluminescent devices”, *IEEE J. Sel. Top. Quantum Electron.*, Vol. 8, No. 4, pp. 749–66, July 2002.
- [74] Myo Thaik, U. Hommerich, R.N. Schwartz, R.G. Wilson, and J.M. Zavada, “Photoluminescence spectroscopy of erbium implanted gallium nitride”, *Appl. Phys. Lett.*, Vol. 71, No. 18, pp. 2641–3, 03 Nov. 1997.
- [75] P.N. Favennec, H. L’Haridon, M. Salvi, D. Moutonnet, and Y. Le Guillou, “Luminescence of erbium implanted in various semiconductors: IV, III-V

- and II-VI materials”, *Electron. Lett.*, Vol. 25, No. 11, pp. 718–19, 25 May 1989.
- [76] J. Heikenfeld, M. Garter, D.S. Lee, R. Birkhahn, and A.J. Steckl, “Red light emission by photoluminescence and electroluminescence from Eu-doped GaN”, *Appl. Phys. Lett.*, Vol. 75, No. 9, pp. 1189–1191, 30 Aug. 1999.
- [77] A.J. Steckl and R. Birkhahn, “Visible emission from Er-doped GaN grown by solid source molecular beam epitaxy”, *Appl. Phys. Lett.*, Vol. 73, No. 12, pp. 1700, 21 Sep. 1998.
- [78] A.J. Steckl, M. Garter, D.S. Lee, J. Heikenfeld, and R. Birkhahn, “Blue emission from Tm-doped GaN electroluminescent devices”, *Appl. Phys. Lett.*, Vol. 75, No. 15, pp. 2184–6, 11 Oct. 1999.
- [79] M. Pan and A.J. Steckl, “Red emission from Eu-doped GaN luminescent films grown by metalorganic chemical vapor deposition”, *Appl. Phys. Lett.*, Vol. 83, No. 1, pp. 9–11, 07 Jul. 2003.
- [80] H.J. Lozykowski, W.M. Jadwisienczak, and I. Brown, “Visible cathodoluminescence of GaN doped with Dy, Er, and Tm”, *Appl. Phys. Lett.*, Vol. 74, No. 8, pp. 1129, 1999.
- [81] Ei Ei Nyein, U. Hommerich, D.S. Lee, J. Heikenfeld, A.J. Steckl, and J.M. Zavada, “Photoluminescence studies of rare earth (Er, Eu, Tm) in situ doped GaN”, *Mat. Sc. and Eng. B: Solid-State Materials for Advanced Technology*, Vol. 105, No. 1-3, pp. 91–96, 15 Dec. 2003.
- [82] A.J. Steckl, J. Heikenfeld, D.S. Lee, and M. Garter, “Multiple color capability from rare earth-doped gallium nitride”, *Mat. Sc. and Eng. B: Solid-State*

- Materials for Advanced Technology*, Vol. 81, No. 1-3, pp. 97–101, 24 Apr. 2001.
- [83] Y.Q. Wang and A.J. Steckl, “Three-color integration on rare-earth-doped GaN electroluminescent thin films”, *Appl. Phys. Lett.*, Vol. 82, No. 4, pp. 502–504, 27 Jan. 2003.
- [84] Jason Heikenfeld and Andrew J. Steckl, “Electroluminescent devices using a high-temperature stable GaN-based phosphor and thick-film dielectric layer”, *IEEE Trans. on Electron Devices*, Vol. 49, No. 4, pp. 557–563, Apr. 2002.
- [85] W.D. Chen, S.F. Song, J.J. Zhu, X.L. Wang, C.Y. Chen, and C.C. Hsu, “Study of infrared luminescence from Er-implanted GaN films”, *Journal of Crystal Growth*, Vol. 268, No. 3-4 SPEC ISS, pp. 466–469, 2004.
- [86] J.H. Kim and P.H. Holloway, “Room-temperature photoluminescence and electroluminescence properties of sputter-grown gallium nitride doped with europium”, *J. Appl. Phys.*, Vol. 95, No. 9, pp. 4787–90, 01 May 2004.
- [87] D.M. Hansen, R. Zhang, N.R. Perkins, S. Safvi, L. Zhang, K.L. Bray, and T.F. Kuech, “Photoluminescence of erbium-implanted GaN and in situ-doped GaN:Er”, *Appl. Phys. Lett.*, Vol. 72, No. 10, pp. 1244, 09 Mar. 1998.
- [88] G.A. Hirata, F. Ramos, R. Garcia, E.J. Bosze, J. McKittrick, O. Contreras, and F.A. Ponce, “A new combustion synthesis method for GaN:Eu³⁺ and Ga₂O₃:Eu³⁺ luminescent powders”, *Phys. Status Solidi A*, Vol. 188, No. 1, pp. 179–82, 16 Nov. 2001.
- [89] A. El-Himri, D. Perez-Coll, P. Nunez, I.R. Martin, V. Lavin, and V.D. Rodriguez, “Preparation and optical spectroscopy of Eu³⁺-doped

- GaN luminescent semiconductor from freeze-dried precursors”, *J. Solid State Chem.*, Vol. 177, No. 11, pp. 4213–20, Nov. 2004.
- [90] H. Wu, C.B. Poitras, M. Lipson, M.G. Spencer, J. Hunting, and F.J. DiSalvo, “Photoluminescence and cathodoluminescence analyses of GaN powder doped with Eu”, *Appl. Phys. Lett.*, Vol. 88, No. 1, pp. 11921–1, 02 Jan. 2006.
- [91] H. Wu, C.B. Poitras, M. Lipson, M. G. Spencer, J. Hunting, and F.J. DiSalvo, “Green emission from Er-doped GaN powder”, *Appl. Phys. Lett.*, Vol. 86, No. 19, pp. 191918, 09 May 2005.
- [92] H. Wu, J. Hunting, C.B. Poitras, M. Lipson, F.J. DiSalvo, and M.G. Spencer, “Visible Light Emission from Er:GaN and Eu:GaN Powder”, *Mat. Res. Soc. Symp. Proc.*, Vol. 872, No. V6.10, 2005.
- [93] C.B. Poitras, H. Wu, A. Turner, M.G. Spencer, and M. Lipson, “Luminescence dynamics and waveguide applications of europium doped gallium nitride powder”, *Appl. Phys. Lett.*, 2006, to be published.
- [94] C. B. Poitras, M. Lipson, H. Wu, and M.G. Spencer, “Luminescence and lifetime properties of europium doped gallium nitride compatible with CMOS technology”, *Mat. Res. Soc. Symp. Proc.*, Vol. 866, No. V3.2, pp. 53–57, 2005.
- [95] H. Wu, J. Hunting, K. Uheda, L. Lepak, P. Konkakaka, F.J. DiSalvo, and M.G. Spencer, “Rapid synthesis of gallium nitride powder”, *J. Cryst. Growth*, Vol. 279, No. 3-4, pp. 303–10, 01 Jun. 2005.
- [96] H. Wu, A. Bourlinos, E.P. Giannelis, and M.G. Spencer, “High quality, low cost continuous poly-GaN film on Si and glass substrates produced by spin

- coating”, *GaN, AlN, InN and Their Alloys. Symposium (Materials Research Society Symposium Proceedings Vol.831)*, pp. 393–8, 2005.
- [97] R.H. Birkhahn, R. Hudgins, D.S. Lee, B.K. Lee, A.J. Steckl, A. Saleh, R.G. Wilson, and J.M. Zavada, “Optical and structural properties of Er³⁺ doped GaN grown by MBE”, *MRS Internet Journal of Nitride Semiconductor Research*, Vol. 4, No. SUPPL 1, pp. 6, 1999.
- [98] C.-W. Lee, H.O. Everitt, D.S. Lee, A.J. Steckl, and J.M. Zavada, “Temperature dependence of energy transfer mechanisms in Eu-doped GaN”, *J. Appl. Phys.*, Vol. 95, No. 12, pp. 7717–7724, 15 Jun. 2004.
- [99] H. Bang, S. Morishima, J. Sawahata, J. Seo, M. Takiguchi, M. Tsunemi, K. Akimoto, and M. Nomura, “Concentration quenching of Eu-related luminescence in Eu-doped GaN”, *Appl. Phys. Lett.*, Vol. 85, No. 2, pp. 227–229, 12 Jul. 2004.
- [100] E.E. Nyein, U. Hommerich, J. Heikenfeld, D.S. Lee, A.J. Steckl, and J.M. Zavada, “Spectral and time-resolved photoluminescence studies of Eu-doped GaN”, *Appl. Phys. Lett.*, Vol. 82, No. 11, pp. 1655–1657, 17 Mar. 2003.
- [101] Z. Li, H. Bang, G. Piao, J. Sawahata, and K. Akimoto, “Growth of Eu-doped GaN by gas source molecular beam epitaxy and its optical properties”, *J. Cryst. Growth*, Vol. 240, No. 3-4, pp. 382–388, May 2002.
- [102] J.S. Im, A. Moritz, F. Steuber, V. Harle, F. Scholz, and A. Hangleiter, “Radiative carrier lifetime, momentum matrix element, and hole effective mass in GaN”, *Appl. Phys. Lett.*, Vol. 70, No. 5, pp. 631–3, 03 Feb. 1997.

- [103] A. Taguchi, K. Takahei, and Y. Horikoshi, “Multiphonon-assisted energy transfer between Yb 4f shell and InP host”, *J. Appl. Phys.*, Vol. 76, No. 11, pp. 7288–95, 01 Dec. 1994.
- [104] A.W. Fang, H. Park, R. Jones, O. Cohen, M.J. Paniccia, and J.E. Bowers, “Heterogeneous Integration of Silicon and AlGaInAs for a Silicon Evanescent Laser”, *Proc. of SPIE*, Vol. 6133, pp. 61330W–1 –8, 2006.
- [105] BeamPROP™ from RSoft Design Group, Inc.
- [106] A. Zhang, Kam Tai Chan, M.S. Demokan, V.W.C. Chan, P.C.H. Chan, and A.H.P. Chan, “Annealing effects on the loss and birefringence of silicon oxynitride rectangular optical waveguides”, *Appl. Phys. Lett.*, Vol. 87, No. 10, pp. 101105–1, 5 Sept. 2005.
- [107] H. Ow, D.R. Larson, M. Srivastava, B.A. Baird, W.W. Webb, and U. Wiesner, “Bright and stable core-shell fluorescent silica nanoparticles”, *Nano Lett.*, Vol. 5, No. 1, pp. 113–17, 17 Dec. 2004.
- [108] C. Poitras, M. Lipson, A. Burns, and U. Wiesner, “Luminescence Enhancement and Inhibition Properties of Core-Shell Silica Fluorescent Nanoparticles”, *Mat. Res. Soc. Symp. Proc.*, Vol. 872, No. J10.5, Spring 2005.
- [109] J.T. Verdeyen, *Laser Electronics*, Pearson Education, 3rd edition, 2000.
- [110] J.D. Jackson, *Classical Electrodynamics*, Wiley, New York, NY, 2nd edition, 1975.
- [111] G.B. Arfken and H.J. Weber, *Mathematical Methods for Physicists*, Academic Press, San Diego, CA, 4th edition, 1995.